

1 **HDAC4 controls senescence and aging by safeguarding the epigenetic identity**
2 **and ensuring the genomic integrity**

3
4
5
6
7
8
9
10
11
12
13
14
15
16
17
18
19

Eros Di Giorgio[§], Harikrishnareddy Paluvai[§], Emiliano Dalla[§], Liliana Ranzino[§], Alessandra
Renzini[#], Viviana Moresi[#], Valentina Cutano[§], Raffaella Picco[§], Claudio Brancolini^{§*}

[§]Department of Medicine, Università degli Studi di Udine, p.le Kolbe 4, 33100 Udine, Italy

[#]DAHFMO Unit of Histology and Medical Embryology, Sapienza University of Rome, via Antonio Scarpa
16, 00161, Rome, Italy

* Address correspondence to: Claudio Brancolini claudio.brancolini@uniud.it

20 **ABSTRACT**

21 The epigenome of senescent cells is characterized by a deep redistribution of H3K27 acetylation.
22 H3K27 is target of class IIa Histone Deacetylases (HDAC4, 5, 7, 9) as part of large repressive complexes.
23 We report here that, among class IIa HDACs, HDAC4 is post-transcriptionally downregulated during
24 senescence and aging. HDAC4 knock-out (KO) triggers premature senescence as a result of two waves of
25 biological events: the accumulation of replication stress (RS) and the expression of inflammatory genes. The
26 latter is achieved directly, through the activation of enhancers (TEs) and super-enhancers (SEs) that are
27 normally monitored by HDAC4, and indirectly, through the de-repression of repetitive elements of retroviral
28 origin (ERVs). The accumulation of DNA damage and the activation of the inflammatory signature influence
29 each other and integrate into a synergistic response required for senescence onset. Our work discloses the
30 key role played by HDAC4 in maintaining epigenome identity and genome integrity.

31

32 **INTRODUCTION**

33 Cellular senescence and aging are complex responses characterized by proliferative arrest and loss of
34 regenerative potential¹. The senescence state is distinguished by a deep epigenetic reprogramming that
35 sculpts the chromatin to maintain cellular survival, arrest the cell-cycle and secrete apocrine and paracrine
36 factors in the presence of consistent DNA damage². In turn, the haploinsufficiency of epigenetic and
37 metabolic regulators increases genome fragility, affects the DNA damage response (DDR) and predisposes
38 to senescence, cell death or malignant transformation³⁻⁷.

39 H3K27ac/H3K27me3 ratio alterations were identified as the driving forces of premature senescence
40 and cancer^{3,7-10}. The balanced action of acetyltransferases (HAT) of the SWI/SNF/p300 complex¹¹ and
41 HDACs of the Sin3, NuRD, CoREST, MiDAC and NCOR complexes¹² controls the acetylation status of
42 H3K27. Class IIa HDACs are catalytically inactive epigenetic readers, quickly recruited on H3K27ac
43 loci^{13,14}, where they monitor the acetylation status through the binding of class I HDACs¹⁵.

44 Here we investigated the role played by class IIa HDACs in the regulation of senescence entrance.
45 The senescence phenotype induced by HDAC4 depletion was studied in detail to unveil the dual role of this
46 epigenetic regulator in preserving genome integrity and in safeguarding regulative elements controlling cell
47 fate.

48

49 **RESULTS**

50 **HDAC4 expression is silenced during cellular senescence and aging.**

51 The epigenetic reprogramming plays key roles in establishing cellular senescence and aging. In this
52 context the contribution of class IIa HDACs has been suggested^{16,17}, but not addressed in a comprehensive
53 manner. Important epigenetic modulators of senescence and aging are down-regulated during the progressive
54 cell cycle arrest^{3,4,18,19}. For this reason, we evaluated class IIa HDACs expression in different models of
55 senescence and aging. HDAC4 and HDAC9, and to a lesser extent HDAC7, were progressively
56 downregulated in human IMR90 fibroblasts undergoing replicative senescence (Fig. 1a/b). As a model of

57 ageing, we compared the protein levels of class IIa HDACs in the dermis and in the liver of young (4
58 months) and old (25 months) mice. HDAC4 and HDAC9 levels decreased, both in aged dermis and liver,
59 whereas HDAC5 decreased only in old dermis (Fig. 1c). Therefore, telomeres attrition in normal cells and
60 physiological aging similarly affected the protein levels of HDAC4 and HDAC9.

61 The delivery in BJ/*hTERT* of the strong oncogenes HRAS^{G12V} or myrAKT1 triggers a premature
62 cell-cycle arrest named oncogene-induced senescence (OIS)^{20,21}. In both models of OIS (Fig.S1a/b), the
63 permanent proliferation arrest is characterized by the post-transcriptional downregulation of HDAC4,
64 HDAC5 and HDAC7, but not of HDAC9 (Fig.1d, S1c,d,h). This trend was also observed in IMR90/*RAS*
65 cells (Fig. S1e).

66 Other oncogenes of viral origin, like E1A and its ΔC -fragment (1-143), are able to overcome OIS, by
67 targeting p16/Rb pathways²². HDAC4/5/9, but not HDAC7, were upregulated by the expression of E1A ΔC
68 in BJ/*hTERT* (Fig.S1c). Moreover, the co-expression of E1A and RAS by-passed the senescent arrest and
69 recovered the protein levels of HDAC4 and HDAC5, but not of HDAC7 (Fig.S1c). Therefore, OIS and OIS
70 escape affect mainly HDAC4 and HDAC5 levels. HDAC4 and HDAC5 were decreased also during stress-
71 induced senescence (SISP) following H₂O₂ treatment and cytokines-induced senescence (Fig.S1f,g,i). In all
72 these conditions, class IIa HDACs are regulated at the post-transcriptional level, except for HDAC9, which
73 transcription is stimulated by oncogenes (Fig. S1c and Table S1).

74 Our preliminary screening identified HDAC4 as the class IIa HDAC member repressed in all tested
75 models of senescence and aging. Most of this downregulation is due to the ubiquitin-proteasome system
76 (UPS) mediated degradation. HDAC4 levels in senescent cells were restored after UPS, but not autophagy
77 inhibition (Fig. S2a/b). Accordingly, HDAC4 was highly poly-ubiquitylated in senescent cells (Fig. 1e). This
78 degradation requires GSK3 β ²³, as the treatment with LiCl (Fig. S2c) and the silencing of GSK3 β restored
79 HDAC4 levels in senescent cells (Fig.1f).

80

81 **The depletion of HDAC4 triggers senescence in different cell types**

82 To investigate the role played by HDAC4 during senescence, we knocked-out HDAC4 in
83 BJ/*hTERT/Ras/E1A* cells, a standard model of OIS escape (Fig.1g and Fig.S2d/e). HDAC4 KO caused the
84 appearance of SA- β -gal positive cells (Fig.1h) and increased the expression of senescence markers
85 (*CDKN1A*, *IL1B*, *IGFBP7*) (Fig.S2f). The induction of senescence in these cells is unrelated to hTERT or
86 E1A levels (Fig. 1g). To confirm the anti-senescence effect of HDAC4, its expression was knocked-out also
87 in low grade leiomyosarcoma cells SK-LMS-1 (Fig.1i and Fig.S2d/e). HDAC4 depletion triggered cell-cycle
88 arrest (Fig.1j) and the appearance of SA- β -gal positive cells (Fig.1k and Fig.S2g). All KO clones failed to
89 grow in semisolid medium, a strong indication of malignancy suppression (Fig.S2h/i). These phenotypes
90 were reproducible in the 4 KO clones generated with 2 different sgRNAs (sg1: 76, 1231; sg2: 205, 1254),
91 while an intermediate phenotype was obtained in the heterozygous clone 275 (Fig. 1j). SK-LMS-1/*HDAC4*^{-/-}
92 cells were also characterized by a moderate induction of cell death (Fig.S2j).

93 *HDAC4*^{-/-} cells were characterized by an altered nuclear morphology (Fig. 1l/m) and the accumulation of
94 γ H2AX foci (Fig. 1n). The re-expression of a Cas9 resistant form of HDAC4 (*HDAC4*^{PAM}) rescued the
95 senescent phenotype in all these clones (Fig. S2k and Fig. 1o), stimulated the entering into the cell-cycle
96 (Fig. 1p), supported their growth in soft agar (Fig. S2l) and reduced the DNA damage levels (Fig. 1q).
97 Similarly, the tamoxifen inducible re-expression of *HDAC4* in SK-LMS-1/*HDAC4*^{-/-} cells (clone 66, +4-
98 OHT) (Fig. 1r) rescued every defect observed in the absence of HDAC4 (-4-OHT) (Fig.1r-v, S2m). As
99 further evidence of senescence induction, SK-LMS-1/*HDAC4*^{-/-} were sensitive to the senolytic drug
100 navitoclax/ABT-263²⁴ (Fig. S3a) and lost the linker histone H1²⁵ and LMNB1²⁶ (Fig. S3b).

101 The premature senescence onset observed in *HDAC4*^{-/-} cells was only partially dependent on MEF2
102 de-repression. In fact, the expression of a super-repressive mutant²⁷ of MEF2 partially restored the
103 proliferation of KO cells (Fig. S3c/d). The appearance of DNA damage and senescence was confirmed in
104 different cellular models (BJ-*TERT/LT*, BJ-*TERT/LT/RAS* and in the melanoma cells WM115) after RNAi-
105 mediated silencing of *HDAC4* (Fig. S3e/f).

106

107 **The transcriptome of *HDAC4*^{-/-} SK-LMS-1 cells is typical of senescent cells**

108 The transcriptomes of four LMS *HDAC4*^{-/-} clones were compared with two control clones
109 (expressing Cas9 or Cas9/sgRNA1 but in which the KO was not achieved) (Fig. S3g). By applying stringent
110 statistical criteria, we identified a minimal signature of 230 genes significantly modulated in all *HDAC4*^{-/-}
111 clones (Fig. 2a,S3g and Table S7). 142 out of 230 of these genes (62%) were induced after HDAC4 deletion
112 (Fig. 2b). An unbiased GSEA analysis identified a senescence geneset among the most enriched in *HDAC4*^{-/-}
113 cells (Fig. 2c). Moreover, senescence-associated secretory phenotype (SASP), Ras-induced senescence (RIS)
114 and NFKB1 target genes were all positively enriched in *HDAC4*^{-/-} (Fig. 2c). Interestingly, in the case of RIS
115 the similarities arose not simply by the SASP but also from the activation of a common epigenetic
116 reprogramming (Fig. S3h).

117 Genome-wide levels of H3K27ac and H3K27me3 showed moderate and focused decreases of H3K27me3
118 and locus specific increases of H3K27ac, at 36h from HDAC4 depletion (Fig. 2d). Interestingly, the re-
119 acetylation observed in *HDAC4*^{-/-} cells involved mainly intronic (18%) and intergenic regions (45%), as
120 similarly observed in other studies^{14,28,29}, while the demethylation occurred close to TSS (Fig.2e).

121 To unveil the contribution of NFKB in this senescent response, we inhibited its activity by introducing IKB α
122 S32A/S36A³⁰ (referred hereinafter as NFKBIA) in *HDAC4*^{-/-} cells. NFKB1 blockage recovered senescence
123 only partially (Fig. 2f-h). In particular, while the expression of SASP genes (*IL1B*, *CXCL8*) strongly depends
124 on NFKB1, the anti-proliferative response (*CDKN1A*, *GADD45A*, *Fbox32/ATROGIN*) was rescued only by
125 HDAC4 (Fig. 2i and S3i). This was confirmed at chromatin level. 2% and 8% of the H3K27ac regions
126 hyper-acetylated in *HDAC4*^{-/-} cells organize the chromatin respectively in: a) typical enhancers (TE) and b)
127 super-enhancers (SE), found activated during senescence (TESs and SESs) (Fig.S3j/k). The latter,
128 exemplified by the *IL1B-IL1A-IL37* SES (Fig.2j), display high preference for NFKB, JUN/AP-1 and MEF2
129 binding (Table S2). The activation of typical enhancers, as well as the increased acetylation and decreased

130 methylation of H3K27 on gene promoters, can control the expression of negative regulators of cell
131 proliferation, as exemplified by the *CDKN1A* locus (Fig. 2k).

132

133 **HDAC4 depletion triggers senescence in melanoma cells.**

134 The best-characterized *in vivo* model of OIS is the human nevus³¹. Among the 18 HDACs, only
135 HDAC4 expression was significantly decreased in nevi and significantly increased in melanomas (Fig. S4a).
136 Moreover, high levels of HDAC4 negatively correlated with patients' survival (Fig. S4b). We therefore
137 knocked-out HDAC4 in A375 melanoma cells. Initially, we obtained only heterozygous clones, suggesting
138 an important role of HDAC4 in regulating cell fitness. Therefore, we generated Dox-inducible cell lines to
139 conditionally express HDAC4^{PAM} before its targeting. With this strategy, five *HDAC4*^{-/-} (320, 304, 401, 150,
140 1090) and two *HDAC4*^{+/-} clones (159, 317) were isolated (Fig. S4c). Similarly to sarcoma cells, HDAC4KO
141 caused the downregulation of LMNB1 (Fig. S4c). A time-course analysis in 304^{-/-} cells evidenced that
142 HDAC4 loss triggered the rapid accumulation of DNA damage and the activation of TP53 (Fig. S4d). A pool
143 of genes up-regulated in SK-LMS-1/*HDAC4*^{-/-} cells turned out to be up-regulated also in A375 *HDAC4*^{-/-}
144 cells (Fig. S4e). Finally, removal of Dox-dependent HDAC4 expression elicited the acquisition of a
145 senescent-like phenotype (Fig. S4f-i). All these phenotypes were weaker in heterozygous clones and the re-
146 expression of HDAC4 rescued the normal phenotype (Fig. S4e-i).

147

148 **Loss of *Hdac4* accelerates senescence in non-transformed cells.**

149 Primary murine embryonic fibroblasts (MEFs) senescence rapidly when grown at atmospheric
150 oxygen, while the maintenance of hypoxic conditions preserves their proliferation³². The conditional (4-OHT
151 dependent) KO of *Hdac4* in MEFs under normoxia sped up the progressive increase in Cdkn2a/p16 levels
152 (Fig. S5a) and the accumulation of DNA damage (Fig. S5b). Similarly, with respect to wt cells, *Hdac4*^{-/-}
153 MEF earlier arrested proliferation (Fig. S5c,d) and switched on a senescence signature (Fig. S5e).

154 We confirmed that MEFs grown in 2% O₂ did not reach senescence, independently from the absence
155 or presence of HDAC4 (Fig. S5f/g). Curiously, after prolonged time of culture, *Hdac4*^{-/-} MEFs evidenced a
156 proliferative crisis from which they rapidly emerged (Fig. S5g).

157

158 **Loss of H1.2 and LMNB1 triggers a second wave of DNA damage in HDAC4^{-/-} cells.**

159 To investigate the timely order of senescence appearance, we took advantage of the *HDAC4*^{-/-}
160 /*HDAC4*^{PAM}-ER cells expressing H1.2-GFP as senescence sensor (Fig. S3b). Apparently, the loss of LMNB1
161 and the accumulation of DNA damage are concomitant events that are coupled to the loss of the linker
162 histone H1 (Fig. 3a). qRT-PCR analysis suggested that the modulation of IGF1 signaling and of the cell-
163 cycle (*CDKN1A*) are early events (Fig. 3b). Immunofluorescence analysis using different markers lead us to
164 define six major phenotypes as exemplified in figure 3c: i) cells positive for H1.2 (H1.2+); ii) cells with a
165 discontinuous (altered) LMNB1 ; iii) cells presenting cytosolic chromatin fragments (CCF⁺); iv) cells with
166 multilobed nuclei; v) cells H1.2 negative (H1.2⁻) with multilobed nuclei and vi) cells with DSBs (γ H2AX⁺).

167 This detailed analysis evidenced that DNA damage increased linearly in the first 48h after HDAC4 removal
168 and exponentially in the next 24h, when the loss of H1.2 and LMNB1 became consistent (Fig. 3d).

169

170 ***In vivo* definition of the early response to HDAC4 depletion.**

171 To gain more insight into the early events triggered by HDAC4 depletion, we introduced in *HDAC4*
172 *^{-/-}HDAC4^{PAM}-ER* cells two reporters (H2B-GFP and Apple-TP53BP1), to monitor mitosis³³ and the
173 accumulation of DNA damage^{34,35} *in vivo*, at single cell level. Unperturbed cells accumulate DNA lesions
174 during interphase, possibly during the proceeding through the S phase. Usually these lesions are resolved in
175 G2, before entering mitosis. After mitosis, cells emerge in G1 with few TP53BP1 positive foci defined as
176 nuclear bodies (TP53BP1-NBs) that could represent under-replicated DNA³⁵⁻³⁷.

177 Cells were monitored over a period of 74 hours from 4-OHT removal/addition by *in vivo* time-lapse confocal
178 microscopy. During this time, 9 out of 10 cells re-expressing HDAC4 entered mitosis twice (Fig. 4). Cell
179 cycle length was constant in these cells (43.22±3.40 hours). The analysis of TP53BP1 dots evidenced the
180 accumulation of DSBs (Supplementary video S1), reflecting the generation of spontaneous DNA or
181 chromatin lesions³⁶. Frequently, small TP53BP1 nuclear foci co-existed with larger TP53BP1-NBs, as
182 previously observed³⁵. The accumulation of all TP53BP1 dots was quantified and represented as a heatmap
183 (Fig. 4 +4-OHT). The pattern of endogenous TP53BP1 distribution in NBs and in small foci was equal to
184 what observed with the fluorescent sensor (Fig.S6a,b,c).

185 HDAC4 removal impaired proliferation. In fact the analyzed cells, with two exceptions (13.2 and
186 19.1), did not enter the second mitosis. Moreover, *HDAC4^{-/-}* cells were characterized by the progressive
187 accumulation of TP53BP1 nuclear foci (Fig. 4 -4-OHT and supplementary movie S2) and by a marked
188 increase in the frequency and dimension of TP53BP1-NBs (Fig. S7). These TP53BP1-NBs were not always
189 symmetrically distributed among sister cells after mitosis (supplementary movie S2). In summary, the
190 absence of HDAC4 exacerbates the trend of DNA lesion accumulation, possibly occurring in late S phase
191 and G2.

192 To correlate the accumulation of pre-mitotic TP53BP1 nuclear dots with mitotic defects, we
193 measured the average number of all TP53BP1 dots for 100 minutes preceding the appearance of
194 chromosomes condensation (mitosis onset). In the presence of HDAC4 the number of TP53BP1 dots was
195 comparable among the analyzed cells (range of 0-3/cell) and the mitosis length was quite homogeneous
196 (100-150 min) (Fig. S6d). A similar behavior was observed during the second mitosis (Fig. S6d). In *HDAC4*
197 *^{-/-}* cells the number of TP53BP1 nuclear dots in G2 was increased, as well as the length of mitosis (Fig. S6d,f).

198 As a consequence of the unresolved chromosomal lesions that are transmitted to daughter cells,
199 TP53BP1-NBs re-emerged in G1³⁶. In the presence of HDAC4, daughter cells emerged with few
200 symmetrical TP53BP1-NBs and this behavior was conserved in the succeeding mitosis (Fig. S6e). In absence
201 of HDAC4 the number of TP53BP1-NBs was increased and they were sometimes asymmetrically distributed
202 between daughter cells. The accumulation of macroscopic nuclear alterations (CCFs, ultrafine DNA bridges

203 (UFBs), lobate nuclei and unproductive mitosis, Fig. S6g) could explain the mitotic delay observed in the
204 absence of HDAC4 (Fig. S6f).

205

206 **ROS and LMNB1 play a minor role in genomic instability of *HDAC4*^{-/-} cells.**

207 Alterations in the nuclear lamina and increased ROS (reactive oxygen species) generation are two
208 possible sources of DNA damage^{38,39}, strongly correlated to senescence onset⁴⁰. LMNB1-GFP was
209 overexpressed in SK-LMS-1/*HDAC4*^{-/-}/*HDAC4*^{PAM}-ER cells cultured in normoxia or in hypoxia to evaluate
210 their separate or joint contribution to HDAC4-mediated senescence. The overexpression of LMNB1 had a
211 partial effect on the appearance of senescence (Fig. 5a) and, while it did not reduce the total number of DNA
212 CCFs, it reduced the appearance of naked (with a defective LMNB1 envelope) CCFs (Fig. 5b). Interestingly,
213 naked CCFs were frequently positive for γ H2AX (arrows and arrowheads Fig. 5b). Accordingly, in LMNB1-
214 GFP cells the increase of γ H2AX signal, observed upon HDAC4 depletion, was slightly reduced (Fig. 5d).
215 Growing the same cells in hypoxia did not affect the accumulation of DNA damage and the appearance of
216 senescence (Fig. 5c/d/e). However, hypoxia modestly potentiated the effects of LMNB1 re-expression in
217 escaping senescence (Fig. 5e). As previously reported⁴¹, LMNB1 re-expression almost completely
218 suppressed SASP, whereas growing cells in hypoxia showed only a modest effect on the expression of
219 *GADD45A* and *CXCL8* (Fig. 5f).

220

221 **DNA lesions occurring during replication accumulate in the absence of HDAC4.**

222 DNA lesions frequently arose during DNA replication. Several intracellular and extracellular
223 conditions can trigger RS and forks stalling or collapsing that lead to DSBs⁴². Damaged replication forks are
224 marked by ATR-mediated hyperphosphorylation of ssDNA-bound RPA32 and by the monoubiquitylation of
225 PCNA. These PTMs are instrumental for the recruitment of repair factors and Pol η ^{43,44}. Starting from 12h
226 after the switch-off of *HDAC4*^{PAM}-ER expression, *HDAC4*^{-/-} cells accumulated Ub-PCNA and phosphorylated
227 (S4/S8) RPA32, which became more evident after 48 hours. These accumulations were paired to the
228 induction of DSBs (Fig. 6a). Most of this DNA damage is due to RS. In fact, inhibition of cell cycle
229 progression, achieved through the CDK4 inhibitor Palbociclib, reduced PCNA ubiquitylation, almost
230 abolished RPA32 phosphorylation and reduced the increase in DSBs (Fig 6b), similarly to HDAC4 re-
231 expression (Fig. 6c). Low doses of aphidicolin (APH) or camptothecin (CPT) can trigger RS^{45,46}. Depletion
232 of HDAC4 showed additive effects to APH or CPT for DSBs accumulation (Fig. 6d-e). Similarly, the
233 recovery after the APH block was delayed by the absence of HDAC4 (Fig. 6f). Overall, these experiments
234 indicate RS as an important source of DNA damage in *HDAC4*^{-/-} cells.

235 *HDAC4*^{-/-} cells did not show evident marks of epigenetic stress that could lead to
236 transcription/replication conflicts⁴⁷⁻⁴⁹ in correspondence of genomic common fragile sites (CFSs)⁵⁰ or early
237 replicating fragile sites (ERFSs)⁵¹. Indeed, some epigenetic alterations fall in CFSs (5.5% with altered
238 H3K27ac and 7.4% with altered H3K27me3) (Fig.6g/h) and, even if they correlate well with the expression
239 of the associated genes ($\rho_{\text{ac(H3K27ac KO/wt)}}=0.37$, $\rho_{\text{me(H3K27me3 KO/wt)}}=-0.32$) (Fig.6i), only 16% of

240 HDAC4-regulated genes (13% up-regulated, 20% down-regulated) fall in CFSs, that cover 15% of the
241 genome. In conclusion, the source of RS that characterizes *HDAC4*^{-/-} cells cannot be ascribed to abrupt
242 epigenetic and transcriptional changes at ERFs and CFSs.

243

244 **HDAC4 depletion causes the activation of ERV transcripts.**

245 Epigenetic perturbations elicit the transcription of ERVs^{52,53} during cellular senescence, aging and
246 cancer^{54,55}. Demethylating agents and HDACi trigger the expression of ERVs^{52,54}. All tested ERVs, with the
247 exception of *ERVWI* that contains a coding gene (*SYCY1*), were induced in *HDAC4*^{-/-} cells (Fig. 6j).
248 Similarly, the IFN response was switched on (Fig. 6j), as a consequence of dsRNAs accumulations (Fig. 6k).
249 The time-course analysis confirmed the up-regulation of ERVs and of the IFN response. The levels of *ERV9*
250 and *ERVFc2* peaked at 60h from HDAC4 removal and then decreased, probably because of an OAS1-
251 dependent degradation (Fig. 7a). The same pattern of ERVs was upregulated during replicative senescence in
252 human fibroblasts (Fig. 7b). ERVs and the IFN response were induced in IMR90-*E1A/RAS* transformed cells
253 after HDAC4 KO (Fig. S8a), in dermis and liver of aged mice (Fig. S8b/c), in *HDAC4*^{-/-} A375 cells (Fig.
254 S8e). ERVs up-regulation was not due to Cas9 activity or nuclear lamina dismantling, as they were
255 unperturbed by the KO of unrelated genes (Fig. S8d) or by the re-expression of LMNB1 in *HDAC4*^{-/-} SK-
256 LMS-1 cells (Fig. S8f). Interestingly, in MCF10A cells the KO of HDAC7, the most abundant class IIa
257 HDAC, induced ERVs expression and this up-regulation was increased in the presence of RAS (Fig. S8g).

258 Importantly, the exogenous delivery of dsRNAs species immunopurified from *HDAC4*^{-/-} cells
259 triggered senescence and cell death in SK-LMS-1 cells (Fig. 7c-e). In *HDAC4*^{-/-} cells, ERVs are
260 characterized by a depletion of H3K27me3 and by an increase in the H3K27ac/H3K27me3 ratio (Fig. 7f).
261 The strong demethylation of K27 of H3 wrapping the genomic DNA of ERVs represents the second most
262 pronounced epigenetic alteration related to HDAC4 removal after the activation of TESs and SESs (Fig. 7g-
263 j).

264

265 **A MAVS/ERV dependent pathway sustains HDAC4-dependent senescence**

266 To better define the contribution of ERVs and of the DDR in this senescence response, we
267 suppressed these pathways by taking advantage of dominant negative (DN) versions of MAVS
268 (*MAVSΔCARD*)⁵⁶ and TP53 (*TP53^{R175H}*)⁵⁷. MAVS was selected since MDA5-RIG1-MAVS recognizes the
269 dsRNA shape of ERV transcripts and triggers the activation of a NFκB/IFN/TNF antiviral responses, which
270 sustain senescence^{58,59}.

271 The expression of TP53-DN and of MAVS-DN in *HDAC4*^{-/-} cells reduced SA-β-gal positivity more
272 efficiently than MEF2-DN (Fig. 8a,h). The impact on counteracting the DDR showed a gradient of efficiency
273 with HDAC4>MAVS-DN>TP53-DN>MEF2-DN (Fig. 8b). The effect of MAVS-DN on DNA damage was
274 unexpected. Hence, we evaluated this suppressive effect in relation to the RS using the CDK4i. Figure 8c
275 shows that MAVS-DN did not completely suppress DNA damage and a stronger effect was observed with
276 the co-expression of HDAC4. As expected, the level of DNA damage was further dropped after the block of

277 the cell cycle operated by CDK4i. This result demonstrates that dsRNA/MAVS are secondary sources of RS
278 that add to the primary and earlier generation, triggered by HDAC4 depletion. The senescence rescue of
279 TP53-DN and MAVS-DN was confirmed by LMNB1 expression (Fig. 8d/e). The role of MAVS in this
280 senescent response was verified by silencing its expression and that of RIG1, using RNAi (Fig. 8f). Next, we
281 evaluated the influences on a pattern of genes (ERVs, SASP, IFNs and cell cycle genes) defining the
282 senescent signature (Fig.8g/h). Re-expression of HDAC4 efficiently rescued all observed alterations.
283 MAVS-DN impacted on SASP and IFN genes, but only partially on cell cycle genes. TP53-DN was
284 ineffective in suppressing ERVs and some SASP genes but effective for the IFN response. LMNB1,
285 NFKBIA and MEF2-DN partially impacted on the senescent signature and mainly at the level of SASP
286 expression (Fig. 8g/h).

287 We confirmed these observations in melanoma A375 cells. MAVS-DN and TP53-DN (more strongly than in
288 SK-LMS-1) inhibited the HDAC4-dependent senescence, rescued LMNB1 levels (Fig. 8i/j) and modulated
289 the senescent signature (Fig. 8k) similarly to what observed in SK-LMS-1 cells.

290

291 **HDAC4 binds and control the acetylation status of super-enhancers**

292 Removal of HDAC4 triggers several dysfunctions including the induction of RS, SEs and the
293 activation of ERVs, which ultimately lead to senescence. Importantly, HDAC4 was still able to repress the
294 senescent signature when CD4Ki was used to induce senescence and cell-cycle arrest with only minimal RS
295 (Fig. 8l). We therefore hypothesized that HDAC4 could act as a safeguard of cell fate by repressing
296 senescent genes. HDAC4 ChIP-seq profile evidenced that HDAC4 binding was highly enriched at the level
297 of specific SE, mainly those activated in senescence (SES) (Fig. 8m). Even though this property is partially
298 shared with the other class IIa HDACs, it particularly marks HDAC4 (Fig. 8m). By binding these SE,
299 possibly through the engagement of transcription factors previously associated with SE like BACH2⁶⁰ and
300 AP-1³ (Fig.8n) and/or MEF2⁶¹ (Table S3), HDAC4 could regulate the expression of BRD4-dependent
301 inflammatory genes (8o,p, Table S4; $\text{pac(H3K27ac KO/wt)}=0.35$ $\text{p}=0.02$ in BRD4 associated³ SESs,
302 $\text{pac}=0.04$ $\text{p}=0.86$ in SESs not associated to BRD4). This response is reinforced and integrated by the H3K27
303 demethylation and subsequent de-repression of ERVs, which engages about 10% of HDAC4 peaks (Fig.
304 8m). In conclusion, HDAC4 has a dual role in regulating senescence, by controlling the replication stress and
305 by repressing directly (SE) or indirectly (through ERV) the inflammatory response.

306

307 **DISCUSSION**

308 We have identified HDAC4 as the class IIa HDAC member downregulated in all the tested models
309 of senescence and aging. GSK3 β ²³ supervises the UPS-mediated degradation of HDAC4 during senescence.
310 HDAC4 depletion forces the senescence entrance in transformed and pre-transformed cells. These responses
311 stem from the activation of two early events: DNA damage and inflammation. *HDAC4*^{-/-} cells become more
312 susceptible to RS. Whether this is due to increased replication fork stalling and collapsing or decreased fork
313 restarting⁶² is presently unknown and deserves further studies. HDAC4-regulated genes falling in CFSs and

314 ERFs underwent normal epigenetic control. This makes it unlikely that a) replication/transcription conflicts⁴⁷
315 arising in these sites or b) other influences of RNA Pol-II on replication origin firing^{48,49} could be at the
316 origin of HDAC4-dependent RS. Interestingly, class I HDACs were found to bind nascent DNA and protect
317 from RS without altering the acetylation of the histones proximal to the fork^{63,64}.

318 HDAC4 depletion elicits H3K27 hyper-acetylation and activation of TE and SE^{3,7} and the H3K27
319 de-methylation and de-repression of repetitive elements of retroviral origin (ERVs)^{52,55}. The activation of
320 these two complementary epigenetic mechanisms confirms that class IIa HDACs are pivotal nodes for the
321 formation of high molecular weight complexes with deacetylase and methyltransferase activities^{65,66}. One
322 third of HDAC4 peaks supervises directly the chromatin remodeling of these elements and promotes the RS-
323 independent activation of a pro-inflammatory signaling. Licensing of SE is emerging as a key aspect of the
324 senescence response^{3,7,60,67}. The activation of this pathway could increase the genomic fragility due to
325 HDAC4 depletion, as demonstrated in other studies^{68,69}. The dismantling of the nuclear lamina and the loss
326 of the linker H1 can further increase transcriptional dysregulation and DNA damage.

327 The complex circuit of events that orbit around HDAC4 demonstrate the centrality of the role played
328 by epigenetic regulators in preserving the correct expression and the integrity of the genome.

329

330 **ACKNOWLEDGEMENTS**

331 We thank Francesca D'Este for the support with the confocal microscope, Danilo Licastro for the support
332 with ChIP-seq experiments and Matteo Corsano for the support with RS experiments. HDAC4 conditional
333 mutant mice were generously provided by Prof. Eric N Olson and Rhonda Bassel-Duby. This study was
334 supported by PRIN 2017 JL8SRX "Class IIa HDACs as therapeutic targets in human diseases: new roles and
335 new selective inhibitors", Interreg Italia- Osterreich rITAT1054 EPIC and the Sarcoma Foundation of
336 America (SFA) to C.B.

337

338 **AUTHOR CONTRIBUTIONS**

339 CB conceived the project. EDG and CB designed and analyzed all experiments. EDG generated all knocked-
340 out cell lines, prepared the libraries for ChIP-seq and performed all gene expression studies. HP completed
341 RNAi experiments and supported EDG in immunoblot experiments. EDG, ED and RF performed
342 bioinformatics analysis. LR performed some western blotting. CB did the confocal microscopy and time-
343 lapse analysis. EDG, HP and CB analyzed the time-lapse experiments. EDG, VC, HP, AR, VM generated
344 cell lines used in the study. EDG, ED and CB interpreted data. CB designed the figures with the help of
345 EDG, ED and RP. EDG and CB wrote the paper.

346

347 **COMPETING INTERESTS STATEMENT**

348 The authors declare no competing interests.

349

350 **REFERENCES**

- 351 1. Ermolaeva, M., Neri, F., Ori, A. & Rudolph, K. L. Cellular and epigenetic drivers of stem cell ageing.
352 *Nat. Rev. Mol. Cell Biol.* **19**, 594–610 (2018).
- 353 2. McHugh, D. & Gil, J. Senescence and aging: Causes, consequences, and therapeutic avenues. *J. Cell*
354 *Biol.* **217**, 65–77 (2018).
- 355 3. Tasdemir, N. *et al.* BRD4 Connects Enhancer Remodeling to Senescence Immune Surveillance.
356 *Cancer Discov.* **6**, 612–629 (2016).
- 357 4. Ito, T., Teo, Y. V., Evans, S. A., Neretti, N. & Sedivy, J. M. Regulation of Cellular Senescence by
358 Polycomb Chromatin Modifiers through Distinct DNA Damage- and Histone Methylation-Dependent
359 Pathways. *Cell Rep.* **22**, 3480–3492 (2018).
- 360 5. Wakita, M. *et al.* A BET family protein degrader provokes senolysis by targeting NHEJ and
361 autophagy in senescent cells. *Nat. Commun.* **11**, 1935 (2020).
- 362 6. Di Micco, R. *et al.* Oncogene-induced senescence is a DNA damage response triggered by DNA
363 hyper-replication. *Nature* **444**, 638–642 (2006).
- 364 7. Sen, P. *et al.* Histone Acetyltransferase p300 Induces De Novo Super-Enhancers to Drive Cellular
365 Senescence. *Mol. Cell* **73**, 684–698.e8 (2019).
- 366 8. Kaneda, A. *et al.* Activation of Bmp2-Smad1 Signal and Its Regulation by Coordinated Alteration of
367 H3K27 Trimethylation in Ras-Induced Senescence. *PLoS Genet.* **7**, e1002359 (2011).
- 368 9. Piunti, A. *et al.* Therapeutic targeting of polycomb and BET bromodomain proteins in diffuse
369 intrinsic pontine gliomas. *Nat. Med.* **23**, 493–500 (2017).
- 370 10. Cruickshanks, H. A. *et al.* Senescent cells harbour features of the cancer epigenome. *Nat. Cell Biol.*
371 **15**, 1495–1506 (2013).
- 372 11. Alver, B. H. *et al.* The SWI/SNF chromatin remodelling complex is required for maintenance of
373 lineage specific enhancers. *Nat. Commun.* **8**, 14648 (2017).
- 374 12. Joshi, P. *et al.* The functional interactome landscape of the human histone deacetylase family. *Mol.*
375 *Syst. Biol.* **9**, 672 (2013).
- 376 13. Stasevich, T. J. *et al.* Regulation of RNA polymerase II activation by histone acetylation in single
377 living cells. *Nature* **516**, 272–275 (2014).
- 378 14. Di Giorgio, E. *et al.* Different class IIa HDACs repressive complexes regulate specific epigenetic
379 responses related to cell survival in leiomyosarcoma cells. *Nucleic Acids Res.* **48**, 646–664 (2020).
- 380 15. Di Giorgio, E. & Brancolini, C. Regulation of class IIa HDAC activities: it is not only matter of
381 subcellular localization. *Epigenomics* **8**, 251–269 (2016).
- 382 16. Marampon, F. *et al.* HDAC4 and HDAC6 sustain DNA double strand break repair and stem-like
383 phenotype by promoting radioresistance in glioblastoma cells. *Cancer Lett.* **397**, 1–11 (2017).
- 384 17. Mason, D. X., Jackson, T. J. & Lin, A. W. Molecular signature of oncogenic ras-induced senescence.
385 *Oncogene* **23**, 9238–9246 (2004).
- 386 18. Chen, J. *et al.* Cathepsin Cleavage of Sirtuin 1 in Endothelial Progenitor Cells Mediates Stress-

- 387 Induced Premature Senescence. *Am. J. Pathol.* **180**, 973–983 (2012).
- 388 19. Zirkel, A. *et al.* HMGB2 Loss upon Senescence Entry Disrupts Genomic Organization and Induces
389 CTCF Clustering across Cell Types. *Mol. Cell* **70**, 730-744.e6 (2018).
- 390 20. Serrano, M., Lin, A. W., McCurrach, M. E., Beach, D. & Lowe, S. W. Oncogenic ras Provokes
391 Premature Cell Senescence Associated with Accumulation of p53 and p16INK4a. *Cell* **88**, 593–602
392 (1997).
- 393 21. Kennedy, A. L. *et al.* Activation of the PIK3CA/AKT Pathway Suppresses Senescence Induced by an
394 Activated RAS Oncogene to Promote Tumorigenesis. *Mol. Cell* **42**, 36–49 (2011).
- 395 22. Deng, Q. *et al.* The Ability of E1A to Rescue ras -Induced Premature Senescence and Confer
396 Transformation Relies on Inactivation of Both p300/CBP and Rb Family Proteins. *Cancer Res.* **65**,
397 8298–8307 (2005).
- 398 23. Cernotta, N., Clocchiatti, A., Florean, C. & Brancolini, C. Ubiquitin-dependent degradation of
399 HDAC4, a new regulator of random cell motility. *Mol. Biol. Cell* **22**, 278–289 (2011).
- 400 24. Inoue-Yamauchi, A. *et al.* Targeting the differential addiction to anti-apoptotic BCL-2 family for
401 cancer therapy. *Nat. Commun.* **8**, 16078 (2017).
- 402 25. Funayama, R., Saito, M., Tanobe, H. & Ishikawa, F. Loss of linker histone H1 in cellular senescence.
403 *J. Cell Biol.* **175**, 869–880 (2006).
- 404 26. Freund, A., Laberge, R.-M., Demaria, M. & Campisi, J. Lamin B1 loss is a senescence-associated
405 biomarker. *Mol. Biol. Cell* **23**, 2066–2075 (2012).
- 406 27. Di Giorgio, E., Hancock, W. W. & Brancolini, C. MEF2 and the tumorigenic process, hic sunt leones.
407 *Biochim. Biophys. Acta - Rev. Cancer* **1870**, 261–273 (2018).
- 408 28. Cutano, V. *et al.* HDAC7-mediated control of tumour microenvironment maintains proliferative and
409 stemness competence of human mammary epithelial cells. *Mol. Oncol.* **13**, 1651–1668 (2019).
- 410 29. Azagra, A. *et al.* In vivo conditional deletion of HDAC7 reveals its requirement to establish proper B
411 lymphocyte identity and development. *J. Exp. Med.* **213**, 2591–2601 (2016).
- 412 30. Wood, K. M., Roff, M. & Hay, R. T. Defective I κ B α in Hodgkin cell lines with constitutively active
413 NF- κ B. *Oncogene* **16**, 2131–2139 (1998).
- 414 31. Michaloglou, C. *et al.* BRAFE600-associated senescence-like cell cycle arrest of human naevi.
415 *Nature* **436**, 720–724 (2005).
- 416 32. Parrinello, S. *et al.* Oxygen sensitivity severely limits the replicative lifespan of murine fibroblasts.
417 *Nat. Cell Biol.* **5**, 741–747 (2003).
- 418 33. Kanda, T., Sullivan, K. F. & Wahl, G. M. Histone–GFP fusion protein enables sensitive analysis of
419 chromosome dynamics in living mammalian cells. *Curr. Biol.* **8**, 377–385 (1998).
- 420 34. Feringa, F. M. *et al.* Persistent repair intermediates induce senescence. *Nat. Commun.* **9**, 3923 (2018).
- 421 35. Spies, J. *et al.* 53BP1 nuclear bodies enforce replication timing at under-replicated DNA to limit
422 heritable DNA damage. *Nat. Cell Biol.* **21**, 487–497 (2019).
- 423 36. Lukas, C. *et al.* 53BP1 nuclear bodies form around DNA lesions generated by mitotic transmission of

- 424 chromosomes under replication stress. *Nat. Cell Biol.* **13**, 243–253 (2011).
- 425 37. Moreno, A. *et al.* Unreplicated DNA remaining from unperturbed S phases passes through mitosis for
426 resolution in daughter cells. *Proc. Natl. Acad. Sci.* **113**, E5757–E5764 (2016).
- 427 38. Graziano, S., Kreienkamp, R., Coll-Bonfill, N. & Gonzalo, S. Causes and consequences of genomic
428 instability in laminopathies: Replication stress and interferon response. *Nucleus* **9**, 289–306 (2018).
- 429 39. Panieri, E. & Santoro, M. M. ROS homeostasis and metabolism: a dangerous liason in cancer cells.
430 *Cell Death Dis.* **7**, e2253–e2253 (2016).
- 431 40. Paluvai, H., Di Giorgio, E. & Brancolini, C. The Histone Code of Senescence. *Cells* **9**, 466 (2020).
- 432 41. Shah, P. P. *et al.* Lamin B1 depletion in senescent cells triggers large-scale changes in gene
433 expression and the chromatin landscape. *Genes Dev.* **27**, 1787–1799 (2013).
- 434 42. Técher, H., Koundrioukoff, S., Nicolas, A. & Debatisse, M. The impact of replication stress on
435 replication dynamics and DNA damage in vertebrate cells. *Nat. Rev. Genet.* **18**, 535–550 (2017).
- 436 43. Olson, E., Nievera, C. J., Klimovich, V., Fanning, E. & Wu, X. RPA2 Is a Direct Downstream Target
437 for ATR to Regulate the S-phase Checkpoint. *J. Biol. Chem.* **281**, 39517–39533 (2006).
- 438 44. Kannouche, P. L., Wing, J. & Lehmann, A. R. Interaction of Human DNA Polymerase η with
439 Monoubiquitinated PCNA. *Mol. Cell* **14**, 491–500 (2004).
- 440 45. Mazouzi, A. *et al.* A Comprehensive Analysis of the Dynamic Response to Aphidicolin-Mediated
441 Replication Stress Uncovers Targets for ATM and ATMIN. *Cell Rep.* **15**, 893–908 (2016).
- 442 46. Puddu, F. *et al.* Chromatin determinants impart camptothecin sensitivity. *EMBO Rep.* **18**, 1000–1012
443 (2017).
- 444 47. Sanchez, A. *et al.* Transcription-replication conflicts as a source of common fragile site instability
445 caused by BMI1-RNF2 deficiency. *PLOS Genet.* **16**, e1008524 (2020).
- 446 48. Brison, O. *et al.* Transcription-mediated organization of the replication initiation program across large
447 genes sets common fragile sites genome-wide. *Nat. Commun.* **10**, 5693 (2019).
- 448 49. Blin, M. *et al.* Transcription-dependent regulation of replication dynamics modulates genome
449 stability. *Nat. Struct. Mol. Biol.* **26**, 58–66 (2019).
- 450 50. Functammasan, A., Walsh, E., Chiaromonte, F., Eckert, K. A. & Makova, K. D. A genome-wide
451 analysis of common fragile sites: What features determine chromosomal instability in the human
452 genome? *Genome Res.* **22**, 993–1005 (2012).
- 453 51. Barlow, J. H. *et al.* Identification of Early Replicating Fragile Sites that Contribute to Genome
454 Instability. *Cell* **152**, 620–632 (2013).
- 455 52. Chiappinelli, K. B. *et al.* Inhibiting DNA Methylation Causes an Interferon Response in Cancer via
456 dsRNA Including Endogenous Retroviruses. *Cell* **162**, 974–986 (2015).
- 457 53. Yu, Y. C.-Y. *et al.* Transient DNMT3L Expression Reinforces Chromatin Surveillance to Halt
458 Senescence Progression in Mouse Embryonic Fibroblast. *Front. Cell Dev. Biol.* **8**, (2020).
- 459 54. Topper, M. J. *et al.* Epigenetic Therapy Ties MYC Depletion to Reversing Immune Evasion and
460 Treating Lung Cancer. *Cell* **171**, 1284–1300.e21 (2017).

- 461 55. Colombo, A. R., Elias, H. K. & Ramsingh, G. Senescence induction universally activates
462 transposable element expression. *Cell Cycle* **17**, 1846–1857 (2018).
- 463 56. Qi, N. *et al.* Multiple truncated isoforms of MAVS prevent its spontaneous aggregation in antiviral
464 innate immune signalling. *Nat. Commun.* **8**, 15676 (2017).
- 465 57. Paluvai, H., Di Giorgio, E. & Brancolini, C. Unscheduled HDAC4 repressive activity in human
466 fibroblasts triggers TP53-dependent senescence and favors cell transformation. *Mol. Oncol.* **12**,
467 2165–2181 (2018).
- 468 58. Gao, L. *et al.* Bone Marrow-Derived Mesenchymal Stem Cells From Patients With Systemic Lupus
469 Erythematosus Have a Senescence-Associated Secretory Phenotype Mediated by a Mitochondrial
470 Antiviral Signaling Protein-Interferon- β Feedback Loop. *Arthritis Rheumatol.* **69**, 1623–1635 (2017).
- 471 59. Ghosh, R., Roy, S. & Franco, S. PARP1 depletion induces RIG-I-dependent signaling in human
472 cancer cells. *PLoS One* **13**, e0194611 (2018).
- 473 60. Vahedi, G. *et al.* Super-enhancers delineate disease-associated regulatory nodes in T cells. *Nature*
474 **520**, 558–562 (2015).
- 475 61. Jin, Y. *et al.* Active enhancer and chromatin accessibility landscapes chart the regulatory network of
476 primary multiple myeloma. *Blood* **131**, 2138–2150 (2018).
- 477 62. Zeman, M. K. & Cimprich, K. A. Causes and consequences of replication stress. *Nat. Cell Biol.* **16**,
478 2–9 (2014).
- 479 63. Wells, C. E. *et al.* Inhibition of Histone Deacetylase 3 Causes Replication Stress in Cutaneous T Cell
480 Lymphoma. *PLoS One* **8**, e68915 (2013).
- 481 64. Kehrl, K. *et al.* Class I Histone Deacetylase HDAC1 and WRN RECQ Helicase Contribute
482 Additively to Protect Replication Forks upon Hydroxyurea-induced Arrest. *J. Biol. Chem.* **291**,
483 24487–24503 (2016).
- 484 65. Cao, C. *et al.* Functional interaction of histone deacetylase 5 (HDAC5) and lysine-specific
485 demethylase 1 (LSD1) promotes breast cancer progression. *Oncogene* **36**, 133–145 (2017).
- 486 66. Di Giorgio, E. *et al.* The co-existence of transcriptional activator and transcriptional repressor MEF2
487 complexes influences tumor aggressiveness. *PLOS Genet.* **13**, e1006752 (2017).
- 488 67. Schäfer, A. *et al.* Impaired DNA demethylation of C/EBP sites causes premature aging. *Genes Dev.*
489 **32**, 742–762 (2018).
- 490 68. Hazan, I., Monin, J., Bouwman, B. A. M., Crosetto, N. & Aqeilan, R. I. Activation of Oncogenic
491 Super-Enhancers Is Coupled with DNA Repair by RAD51. *Cell Rep.* **29**, 560-572.e4 (2019).
- 492 69. Chang, Y.-H. & Dubnau, J. The Gypsy Endogenous Retrovirus Drives Non-Cell-Autonomous
493 Propagation in a Drosophila TDP-43 Model of Neurodegeneration. *Curr. Biol.* **29**, 3135-3152.e4
494 (2019).
- 495 70. Cersosimo, U. *et al.* Synthesis, Characterization, and Optimization for in Vivo Delivery of a
496 Nonselective Isopeptidase Inhibitor as New Antineoplastic Agent. *J. Med. Chem.* **58**, 1691–1704
497 (2015).

- 498 71. Marzagalli, M., Casati, L., Moretti, R. M., Montagnani Marelli, M. & Limonta, P. Estrogen Receptor
499 β Agonists Differentially Affect the Growth of Human Melanoma Cell Lines. *PLoS One* **10**,
500 e0134396 (2015).
- 501 72. Clocchiatti, A. *et al.* The MEF2-HDAC axis controls proliferation of mammary epithelial cells and
502 acini formation in vitro. *J. Cell Sci.* **128**, 3961–3976 (2015).
- 503 73. Ciotti, S. *et al.* GSK3 β is a key regulator of the ROS-dependent necrotic death induced by the
504 quinone DMNQ. *Cell Death Dis.* **11**, 2 (2020).
- 505 74. Potthoff, M. J. *et al.* Histone deacetylase degradation and MEF2 activation promote the formation of
506 slow-twitch myofibers. *J. Clin. Invest.* **117**, 2459–2467 (2007).
- 507 75. Nam, Y.-J. *et al.* Induction of diverse cardiac cell types by reprogramming fibroblasts with cardiac
508 transcription factors. *Development* **141**, 4267–4278 (2014).
- 509 76. Di Giorgio, E., Gagliostro, E., Clocchiatti, A. & Brancolini, C. The Control Operated by the Cell
510 Cycle Machinery on MEF2 Stability Contributes to the Downregulation of CDKN1A and Entry into
511 S Phase. *Mol. Cell. Biol.* **35**, 1633–1647 (2015).
- 512 77. Peruzzo, P. *et al.* Transformation by different oncogenes relies on specific metabolic adaptations. *Cell*
513 *Cycle* **15**, 2656–2668 (2016).
- 514 78. Paroni, G. *et al.* Caspase-dependent regulation of histone deacetylase 4 nuclear-cytoplasmic shuttling
515 promotes apoptosis. *Mol Biol Cell* **15**, 2804–2818 (2004).
- 516 79. Muellera, S. *et al.* RNAi-mediated immunity provides strong protection against the negative-strand
517 RNA vesicular stomatitis virus in drosophila. *Proc. Natl. Acad. Sci. U. S. A.* (2010).
518 doi:10.1073/pnas.1014378107
- 519 80. Lasry, A. & Ben-Neriah, Y. Senescence-associated inflammatory responses: Aging and cancer
520 perspectives. *Trends in Immunology* **36**, 217–228 (2015).
- 521 81. Cerami, E. *et al.* The cBio Cancer Genomics Portal: An open platform for exploring
522 multidimensional cancer genomics data. *Cancer Discov.* **2**, 401–404 (2012).
- 523 82. Jiang, Y. *et al.* SEDb: A comprehensive human super-enhancer database. *Nucleic Acids Res.* (2019).
524 doi:10.1093/nar/gky1025
- 525 83. Paces, J. HERVd: the Human Endogenous RetroViruses Database: update. *Nucleic Acids Res.* **32**,
526 50D – 50 (2004).
- 527 84. Kumar, R. *et al.* HumCFS: a database of fragile sites in human chromosomes. *BMC Genomics* **19**,
528 985 (2019).
- 529 85. Eisenberg, E. & Levanon, E. Y. Human housekeeping genes, revisited. *Trends Genet.* **29**, 569–574
530 (2013).
- 531 86. Whyte, W. A. *et al.* Master Transcription Factors and Mediator Establish Super-Enhancers at Key
532 Cell Identity Genes. *Cell* **153**, 307–319 (2013).
- 533 87. Quinlan, A. R. & Hall, I. M. BEDTools: a flexible suite of utilities for comparing genomic features.
534 *Bioinformatics* **26**, 841–842 (2010).

535 88. Bailey, T. L., Johnson, J., Grant, C. E. & Noble, W. S. The MEME Suite. *Nucleic Acids Res.* **43**,
536 W39–W49 (2015).

537

538 **METHODS**

539 **Cell culture and reagents.**

540 BJ/hTERT and IMR90 cells (previously characterized⁵⁷), SK-LMS-1 (*TP53*^{wt/G245S}) and SK-UT-1
541 leiomyosarcoma cells (previously characterized¹⁴), HEK293T, LinXE, Ampho Phoenix and MEF
542 *HDAC4*^{loxp/loxp} cells were cultured as previously described¹⁴ in 10% FBS DMEM (Euroclone). A375⁷⁰
543 (*TP53*^{wt/wt}) and WM115⁷¹ (*TP53*^{wt/wt}) melanoma cells were grown in RPMI, MCF10A were grown as
544 previously described⁷². MCF10A/*HDAC7*^{-/-}, U87MG/*GSK3β*^{-/-}, SK-UT-1/*HDAC4*^{-/-} and *HDAC9*^{-/-} were
545 previously described^{14,28,73}. For the conditioning of BJ/hTERT cells, the medium obtained from
546 BJ/hTERT/*HRAS*^{G12V} or *HYGRO* cells cultured in 60mm plates for 8 days, was filtered and diluted 1:1 with
547 fresh medium and used to treat cells twice for 96h, with a change after 48h. For the experiments performed
548 in Hypoxia, cells were grown in hypoxic chambers at 37°C, 5% CO₂, 2% O₂ (Baker Ruskinn). The following
549 chemicals were used: 250nM 4-OHT (Sigma-Aldrich), 1μM Doxycycline (Sigma-Aldrich), 1μM MG132
550 (Sigma-Aldrich), 10μM Chloroquine (Sigma-Aldrich), 0.4% Trypan Blue (Sigma-Aldrich), 200μM H₂O₂
551 (Sigma-Aldrich), 1μM PD0332991 (Sigma-Aldrich), 500nM Aphidicolin (Sigma-Aldrich), 3.125μM
552 Camptothecin (Enzo Life Sciences), 20μM Etoposide (Enzo Life Sciences), 100nM ABT-263
553 (Clinisciences).

554

555 **Generation and culture of *Hdac4*^{fl/fl} and *Hdac4*^{-/-} murine embryonic fibroblasts**

556 *Hdac4*^{fl/fl} mice were previously described⁷⁴. MEFs were generated following standard procedures⁷⁵ from 13.5
557 days-old embryos. Single cell suspensions were expanded in DMEM/10% FBS in hypoxia. 5*10⁶ cells were
558 retrovirally infected to express Cre-ER. Not infected cells were removed from culture by puromycin
559 (2μg/ml, Sigma-Aldrich) selection. The recombination was achieved through the treatment for 48h with 4-
560 OHT (Sigma-Aldrich). At the end of this incubation, half of the culture was kept in normoxia and half in
561 hypoxia. At each splitting the total number of cells was counted (Countess II, LifeTechnologies) and the
562 doubling time (dt) was calculated as previously described⁷⁶.

563 **Plasmid construction, transfection, retroviral and lentiviral infection, silencing**

564 pLENTI-CRISPR/V2 (Plasmid #52961), pSpCas9(BB)-2A-GFP(PX458) (Plasmid #48138), pSpCas9(BB)-
565 2A-Puro (PX459) (Plasmid #62988), pCW-Cas9 (Plasmid #50661), pCW57/Hygro-MCS1-2A-MCS2
566 (Plasmid #80922), *Apple-53BP1trunc* (Plasmid #69531), *pEGFP-N1/H2B-GFP* (Plasmid #11680), pBabe-
567 *Puro-IKBalpha* (NFKBIA) S32A/S36A (Plasmid #15291), MSCV-CreERT2-Puro (Plasmid #22776) were
568 obtained from Addgene. pLKO-Puro *shHDAC4* 1 (TRCN0000314667) and 2 (TRCN000004832) were
569 obtained from Sigma-Aldrich. pWZL-Hygro-*HDAC4*^{PAM} (V31L or P16A), pWZL-Hygro-*HDAC4*^{PAM}-ER
570 pCW-Hygro- *HDAC4*^{PAM} were obtained by sub-cloning a mutagenized HDAC4 (QuikChange Site-Directed
571 Mutagenesis Kit, Agilent) into the linearized empty backbones by a restriction-based approach. *Apple-*

572 *53BP1trunc* and *H2B-GFP* were sub-cloned respectively in pBABE-*Zeo* and pWZL-*Neo*, NFKBIA-
573 S32A/S36A into pWZL-*Neo-GFP*. pWZL-*Neo-MCS1-2A-MCS2* was obtained by sub-cloning the MCS of
574 pCW57 *Hygro MCS1-2A-MCS2* into pWZL-*Neo* through a recombination-based approach. The generated
575 plasmid was used as acceptor vector for the cloning of *HRAS*^{G12V} (*NheI/SalI*) and *E1A/1-143* (*MluI/BglII*-
576 *BamHI*) to generate pWZL-*Neo-HRAS/G12V-2A-E1A 1-143*. pWZL-*Neo/GFP-LMNBI*, pWZL-*Neo*-
577 *MAVSDN*(Δ CARD 1-100), pBABE-*Zeo-MAVSDN* and pWZL-*Neo/HI.2-GFP* were obtained by amplifying
578 the relative cDNAs from IMR90 cells. pWZL-*Hygro-MEF2/ENG*, pWZL-*Hygro-HRAS*^{G12V}, pBABE-*Puro*-
579 *HRAS*^{G12V} and pBABE-*Puro-myrAKT1* were previously described⁵⁷. pCW-*Puro-HRAS*^{G12V} and *myrAKT1*
580 were obtained by subcloning. pLKO-*Hygro* plasmid expressing the same shRNAs were obtained by oligo
581 cloning. All the generated plasmids were checked by restriction and sequencing. The primers used for
582 cloning are listed in Table S5. Transfections, viral infections and siRNA delivery were done as previously
583 described^{28,77}. The following siRNAs (148 pmol) were used: HDAC4
584 (CCACCGGAAUCUGAACCACUGCAUU, Invitrogen Stealth), MAVS 1
585 (CCACCUUGAUGCCUGUGAA), MAVS 2 (CAGAGGAGAAUGAGUAUA), RIG-1
586 (AAUUCAUCAGAGAUAGUCA).

587

588 **CRISPR/Cas9 Genome editing**

589 SpCas9 was stably transduced to generate SK-LMS1 *HDAC4*^{-/-} clones (76,1231,205,1254,66), *HDAC4*^{+/-}
590 clone 275 and BJ/E1A-RAS *HDAC4*^{-/-}. SpCas9 was transiently transfected (Lipofectamine 2000,
591 LifeTechnologies) to generate SK-LMS-1 *HDAC4*^{-/-} clones (635, 273, 274, 275, 277, 279), A375 *HDAC4*^{-/-}
592 clones (304, 401, 150, 1090) and *HDAC4*^{+/-} clones (317, 159). A Cas9 resistant HDAC4 (PAM mutated,
593 using a strategy previously described²⁸), was stably expressed prior to the KO (in SK-LMS-1 clones
594 273,274,275, 277, 279) or continuously re-expressed in a 4-OHT dependent (SK-LMS-1 clone 66) or DOX
595 dependent (A375 clones 304, 401, 150, 1090) manner. The sgRNA used are listed in Table S5. Monoclonal
596 cultures were generated by seeding n=1 (SK-LMS-1 and A375), n=3 (BJ/E1A-RAS) cells in each well of 96-
597 well plates (Sarstedt). The successful generation of KO clones was screened by immunoblotting and
598 confirmed by Sanger sequencing.

599 **Immunofluorescence and immunoblotting**

600 Cells were fixed with 3% paraformaldehyde and permeabilized with 0.3% Triton X-100. The secondary
601 antibodies were Alexa Fluor 488-, 546- or 633-conjugated anti-mouse and anti-rabbit secondary antibodies
602 (Molecular Probes). Actin was labelled with phalloidin-AF546 or AF-660 (Molecular Probes). For the
603 intracellular staining of dsRNA, the permeabilization step was performed for 5' with 0.5% Triton X-100.
604 ICC blocking solution (3% w/v BSA (Sigma-Aldrich), 3% v/v goat serum (Abcam), 0.02% v/v Tween-20 in
605 PBS) was applied for 1h to block nonspecific binding and for the incubation at 37°C for 1h with 250 ng J2
606 antibody (Scicons). For S phase analysis, cells were grown for 3 h with 50 μ M Bromodeoxyuridine (BrdU).
607 After fixation, coverslips were treated with HCl (1% and 2%), quenched with Borate and processed for

608 immunofluorescence. Cells were imaged with a confocal microscope Leica AOBS SP8 or with Leica
609 AF6000 LX. Nuclei were stained with Hoechst 33258 or DAPI (Sigma-Aldrich).

610 Cell lysates after SDS-PAGE and immunoblotting on nitrocellulose (Whatman) were incubated with primary
611 antibodies. HRP-conjugated secondary antibodies were obtained from Cell Signalling and blots were
612 developed with Super Signal West Dura (Thermo Fisher Scientific). Primary and secondary antibodies were
613 removed by using Restore PLUS Western Blot Stripping Buffer (Thermo Fisher Scientific), according to
614 manufacturer. Unless otherwise indicated, all the immunoblot figures were representative of at least two
615 biological replicates. The primary and secondary antibodies used in this work are listed in Table S6. Images
616 represent maximum intensity projections of 3D image stacks and were adjusted for brightness and contrast
617 for optimal visualization.

618 **Time-lapse video microscopy**

619 SK-LMS-1 and SK-LMS-1/*HDAC4*^{-/-}/*HDAC4*^{PAM}-ER cells engineered to express H2B-GFP and Apple-
620 53BP1 trunc or H2B-GFP alone were seeded on fibronectin coated 35mm Glass bottom dishes (MatTek) at
621 low density (0.3×10^5 cells). After 24h, medium was refreshed and 4-OHT was added in HDAC4 re-
622 expressing cells. 6h later, the dishes were housed in the live cell imaging chamber of a Leica AOBS SP8
623 confocal microscopy, maintained in a humidified atmosphere at 37°C and 5%CO₂ and imaged every 10
624 minutes for 74h under four dimensions. 5 z-stacks were collected for each time-point. Laser power, exposure
625 time, pinhole aperture and acquisition intervals were chosen appropriately to minimize toxicity and
626 bleaching.

627 **Proteomics and transcriptomics from *in vivo* murine aging models**

628 C57BL/6J female mice were obtained from Shared Ageing Research Models (ShARM, UK). Tissues
629 explanted from 4 months (128 days) and 26 months (774 days) old mice were snap-frozen in liquid nitrogen.
630 For protein lysates generation, subsections of the liver and of the skin were grinded into a powder with a
631 pestle and lysed for 1h at 4°C respectively with 400 and 200µl RIPA lysis buffer for 10mg of tissue. 4x
632 Laemli sample buffer was added to the clarified lysates and after boiling the samples were loaded on
633 SDS/PAGE gels. For RNA extraction, 1ml Tri Reagent (Molecular Research Center) was added to 10mg of
634 smashed tissues. After 1h incubation at 4°C, RNA was recovered by phenol-chloroform extraction/ethanol
635 precipitation and resuspended in 20 µL RNase-free water.

636 **Immunoprecipitation**

637 Cells were lysed for 10' into hypotonic lysis buffer (20mM Tris-HCl pH7.4, 10mM KCl, 10mM MgCl₂, 1%
638 Triton X-100, 10% glycerol, 50mM Iac, 1 mM phenylmethylsulphonylfluoride, 5 mM NaF, 1 mM Na₃VO₄),
639 supplemented with protease inhibitors and 10µM MG-132 and 10µM G5. Lysates were incubated for 5 h
640 with 1µg anti-HDAC4⁷⁸ or rabbit IgG and for 1h with 30µl slurry protein A (GE). After 4 washes, the
641 immunocomplexes were reversed with 2x Laemli sample buffer, boiled, resolved by SDS-PAGE and
642 subjected to western-blotting. 1/100 of total lysate has been collected as input.

643 **dsRNA immunoprecipitation**

644 Total RNA was extracted with Tri Reagent (Molecular Research Center) from a pellet of 35×10^6 SK-LMS-1
645 HDAC4 KO cells. IP was performed O/N in Polysomal Lysis Buffer⁷⁹ in the presence of 10 μ g J2 antibody
646 (Scicons). 50 μ l slurry protein A (GE) was added and incubated in continuous rotation at 4°C for 4h. After 5
647 washes of the collected immunocomplexes, RNA was recovered by phenol-chloroform extraction/ethanol
648 precipitation and resuspended in 20 μ l RNase-free water. The precipitation was repeated until a final amount
649 of 1.6 μ g of purified RNA was reached. 800ng were treated for 20' at 37°C with 50u ShortCut Rnase III
650 (NEB), in the digestion buffer supplied by the manufacturer. The digestion was stopped with 10x EDTA.
651 The remaining 800ng were treated in the same manner but without the addition of RNase III. 30pmoles of
652 purified dsRNA treated or not with RNaseIII were transfected in recipient cells, by using 15 μ l
653 Lipofectamine 3000 (LifeTechnologies) and 250 μ l Optimem (Gibco). The enrichment of dsRNA in the
654 preparation was evaluated by qPCR and expressed as % of enrichment over input.

655 SA- β -gal assay

656 Cells seeded on coverslips in 12-well plates were fixed for 5' (PBS 2% formaldehyde/0.2% glutaraldehyde),
657 washed twice with 0.9% NaCl and stained for 16h at 37°C with staining solution: 40 mM citric acid/Na
658 phosphate buffer, 5 mM K₄[Fe(CN)₆]3H₂O, 5 mM K₃[Fe(CN)₆], 150 mM sodium chloride, 2 mM
659 magnesium chloride and 1 mg/mL X-gal (Panreact Applichem). Images were acquired with Leica LD bright
660 field optical microscope.

661 Transformation assay

662 Soft agar assay was performed as previously described^{57,77}. Briefly, a total of 0.8×10^5 cells were seeded in
663 0.3% top agar/DMEM layer above a 0.6% agar/DMEM basement. Fresh medium was added twice/week.
664 After 15 days of culture the supernatant was discarded and the MTT [3-(4,5-dimethylthiazol-2-yl)-2,5-
665 diphenyltetrazolium bromide] staining (0.5mg/ml in PBS) was applied for 2h. Images were acquired with a
666 Leica DN6000 microscope. Foci were automatically counted with Clono Counter.

667 RNA extraction and quantitative qRT-PCR

668 Cells were lysed using Tri Reagent (Molecular Research Center). 1.0 μ g of total RNA was DNaseI treated
669 (NEB #T2010) and retro-transcribed by using 100 units of M-MLV Reverse transcriptase (Life
670 Technologies) in the presence of 1.6 μ M oligo(dT) (Sigma-Aldrich) and 4 μ M Random hexamers
671 (Euroclone). qRT-PCRs were performed using SYBR green technology (KAPA Biosystems). Data were
672 analyzed by comparative threshold cycle (delta delta Ct) using *HPRT* and *GAPDH* or *ACTB* and *GAPDH* as
673 normalizer. The primers used for qRT-PCR are listed in Table S5.

674 RNA array expression and data analysis

675 Total RNA was purified with Quick-RNA Miniprep (ZymoResearch), amplified according to the
676 specifications of the Illumina TotalPrep RNA Amplification Kit (Ambion) and hybridized on Illumina
677 whole-genome HumanHT-12 v 4.0 chip (Illumina). Acquisition and data analysis were performed as
678 previously described¹⁴. Principal component analysis (PCA) was performed by using R function pcomp.
679 Differentially expressed genes (DEGs) were called accordingly to the following criteria: |fold change|>2 and

680 p adj.<0.05. The list of the DEGs is provided as Table S7. GSEA analysis in Fig.2 was performed as
681 previously described¹⁴. The transcripts defining the “NFκβ”, “SASP”⁸⁰ and “RIS up-regulated genes” gene
682 sets are listed in Table S8. Gene list enrichment in Table S4 was performed by interrogating MSigDB
683 collections (BP,C6,CGP,H,MF) with the transcripts associated to promoters (with 2kb from TSS), TEs or
684 SEs bound by HDAC4; the obtained enrichments were considered significant for p and FDR <0.05 and if at
685 least three Gene Sets fall in the same category. For the expression levels and Kaplan-Meier analysis of
686 TCGA Skin Cutaneous Melanoma samples, data were retrieved from CBioPortal⁸¹ and expressed as z-score.
687 Z-scores > |1.75| were selected as cut-off. For bioinformatics analysis in Fig.2, 7, S3 and S4, the following
688 GEO datasets were analyzed: GSE38410, GSE74324, GSE40349, GSE3189, GSE78138, GSE45276,
689 GSE36640, GSE40349, GSE132569.

690

691 **ChIP, library construction, ChIP-seq and NGS data analysis**

692 Chromatin was obtained from SK-LMS-1 cells, 36h after or not HDAC4 removal, and immunoprecipitated
693 with 2 μg of anti-H3K27ac, 3μg of anti-H3K27me3, 4μg of anti-LMNB1 and 4μg of anti-HDAC4 antibodies
694 or control IgG, as previously described¹⁴. Three independent biological replicates were pulled according to
695 BLUEPRINT requirements and 5 ng of total DNA were used to prepare ChIP-seq libraries, according to
696 TruSeq ChIP Sample Preparation guide (Illumina). Libraries were sequenced on the Illumina HiSeq 2000
697 sequencer. The ShortRead R/Bioconductor package was used to evaluate the quality of sequencing reads and
698 Bowtie 2 was used to align them to NCBI *GRCh38* human genome reference. Peak calling was performed
699 against input sequences using HOMER for HDAC4 ChIP (“factor” mode) and MACS2 for H3K27ac and
700 H3K27me3 (“sharp” mode and “broad” mode, respectively); gene annotations were performed as previously
701 described¹⁴. gplots, biomaRt and Gviz R/Bioconductor packages and the deepTools suite were used to
702 generate peak heatmaps and for the visualization of genomic loci. The H3K27ac and H3K27me3 enriched
703 genomic regions between HDAC4 KO and wt were called according to $\sum_{k=peak}^{\pm 15000} f(k)$, where $f(k) =$
704 $\frac{enrichment\ KO}{enrichment\ wt} \cdot |\log_2(Fc)| \geq 1$ was used as cut-off. The following databases were consulted for the dissection of
705 the ChIP-seq peaks as reported in Fig.6g/h, 7g/h, 8m, S3j/k: SEdb⁸² for super-enhancers, HERVd⁸³ for
706 endogenous retroviruses, HumCFS⁸⁴ and the refinement⁵⁰ for common fragile sites; ERFs⁵¹ and HK exons⁸⁵.
707 sample_01_066_SE of smooth muscle SE was used as lineage reference. “SES”, defined according to the
708 ROSE algorithm⁸⁶, represents the SEs activated during senescence. SES is the union of the SE identified
709 during OIS³ and replicative senescence⁷ and is provided as Table S9. Liftover tool was used to convert
710 genome coordinates between assemblies and to remap homologous sequences between genomes. The
711 bedtools toolset (--intersect option)⁸⁷ was used to identify overlaps of at least one nucleotide. The
712 investigated classes of genomic elements have been considered as separated, not redundant and not
713 overlapping. The enrichment has been calculated with respect to the genome coverage of each genomic
714 element (length of female haploid human genome: 3184709445 nucleotides). Known and novel motif
715 discovery was performed using the MEME-ChIP tool from the MEME Suite⁸⁸. The following parameters
716 were used: -ccut 0; -order 1; -meme-maxsize 100000000; -meme-minsites 2; -meme-maxsites 100; -meme-

717 minw 6; -meme-maxw 10; -meme-nmotifs 10; -meme-mod anr; -dreme-e 0.05; -centrimo-score 5.0; -
718 centrimo-ethresh 10. The identified enriched motifs were compared to the Jolma2013,
719 JASPAR2018_CORE Vertebrates_non_redundant and uniprobe_mouse databases for annotation. Enrichr
720 (TRRUST) (<http://amp.pharm.mssm.edu/Enrichr/>) was used for the motif enrichment analysis in Table S2.

721 Statistics

722 For experimental data, Student t-test was employed. Mann–Whitney test was applied when normality could
723 not be assumed. $p < 0.05$ was chosen as statistical limit of significance. For comparisons between more than
724 two samples, the Anova test was applied coupled to Kruskal–Wallis and Dunn’s Multiple Comparison Test.
725 For correlation between two variables, Pearson correlation or Spearman correlation were calculated for
726 normal or non normal distributions, respectively. Excel and GraphPad Prism were used for routine
727 analysis, R/Bioconductor packages for large data analysis and heatmap generation. We marked with
728 $*p < 0.05$, $**p < 0.01$, $***p < 0.001$. Unless otherwise indicated, all the data in the figures were represented as
729 arithmetic means \pm the standard deviations from at least three independent experiments.

730 Data availability

731 Raw data corresponding to ChIP-seq experiments are uploaded with GEO accession GSE149644.
732 For reviewers, to access the data, <https://www.ncbi.nlm.nih.gov/geo/query/acc.cgi?acc=GSE149644>
733 Enter token clyvsuiwrlqfrgn into the box.

734

735 FIGURES LEGENDS

736 **Figure 1. HDAC4 is dysregulated during senescence and aging and is required for senescence escape.**

737 **a.** Immunoblot analysis in IMR90 cells undergoing replicative senescence. Actin was used as loading
738 control. **b.** Microscopic images of SA- β -gal stained IMR90 cells (scale bar 50 μ m). **c.** Immunoblot analysis
739 in tissue-derived lysates obtained from C57BL/6J female mice sacrificed at 128 (young) and 774 (old) days
740 of age. Actin was used as loading control. **d.** Immunoblot analysis in BJ/*hTERT* expressing the indicated
741 transgenes for the indicated time. Vimentin was the loading control. **e.** Cellular lysates obtained in BJ/*hTERT*
742 expressing for 8 days the indicated transgenes and treated or not for 8h with MG132 were
743 immunoprecipitated using anti-HDAC4 and immunoblotted with the indicated antibodies. **f.** Immunoblot
744 analysis in BJ/*hTERT* cells expressing HRAS^{G12V} and silenced for GSK3 β , as indicated. **g.** Immunoblot
745 analysis in BJ/*hTERT/E1A/RAS/HDAC4*^{+/+} or ^{-/-} cells, as indicated. Actin was used as loading control. **h.**
746 Analysis of the senescent cells as scored after SA- β -gal staining. Mean \pm SD; n = 3. **i.** Immunoblot analysis
747 in SK-LMS-1/*HDAC4*^{+/+} or ^{-/-} as indicated. **j.** Cell-proliferation curve of the indicated *HDAC4*^{+/+}, ^{+/-}, ^{-/-} SK-
748 LMS-1 cells. Mean \pm SD; n = 4. **k.** Analysis of the senescent cells as scored after SA- β -gal staining. Mean \pm
749 SD; n = 4. **l.** Representative image of normal and altered DAPI-stained nuclei observed in SK-LMS-1
750 *HDAC4*^{-/-} cells (scale bar 10 μ m). **m-n.** Analysis of the % of cells displaying altered nuclei or γ H2AX foci
751 (>5). Etoposide was a control (2h, 20 μ M). Mean \pm SD; n = 4. **o-p-q.** Analysis of SA- β -gal (o), BrdU (p) and
752 γ H2AX (q) positivity in wt or HDAC4 KO cells expressing HYGRO^R (clone 635) or HDAC4^{PAM}. Mean \pm

753 SD; n = 4. The significance is relative to clone 635. **r.** Immunoblot analysis in SK-LMS-1 wt or KO (clone
754 66) cells re-expressing a tamoxifen inducible *HDAC4^{PAM}-ER*. Arrowheads point to HDAC4 cleavage
755 products observed in HDAC4-ER expressing cells. Actin was the loading control. **s-v.** Analysis of SA- β -gal
756 (s), BrdU (t), nuclear alteration (u) and γ H2AX (v) positivity in the indicated cells. Mean \pm SD; n = 4.

757 **Figure 2. HDAC4 depletion causes a senescence-like transcriptional and epigenetic reprogramming. a.**
758 Venn diagrams showing the number of transcripts differently regulated in SK-LMS-1/*HDAC4^{-/-}* cells
759 generated by using two different sgRNAs (green and red). Differentially expressed genes (DEGs) were
760 selected based on $|\text{fold change}| > 2$ and $p < 0.05$. **b.** Heat-map of the absolute expression levels of the DEGs in
761 the indicated clones and biological replicates hierarchically clustered accordingly to average linkage. Blue
762 shades intensity is proportional to transcripts abundance. **c.** GSEA plots displaying the NES obtained by
763 interrogating the transcriptome of HDAC4 wt and KO cells with the indicated gene sets. **d.** (Upper) Heat-
764 map of the 97831 H3K27ac and 139200 H3K27me3 enriched peaks in the indicated SK-LMS-1 cells;
765 (Lower) Heat-map of the 4441 H3K27ac peaks displaying a FPKM (KO/wt) >2 and of the 1205 H3K27me3
766 peaks displaying a FPKM (wt/KO) >2 (FC >2), in a region of ± 15 Kb around peak summit. **e.** Genomic
767 distribution of all the H3K27ac and H3K27me3-enriched peaks (top panel), or only of those associated with
768 a FC >2 , as indicated and shown in Fig. 2d. **f-g-h.** Analysis of BrdU (f), SA- β -gal (g) and γ H2AX (h)
769 positivity in wt or HDAC4 KO cells expressing HYGRO^R (clone 635) or GFP-NFKBIA (clones 55 and 70).
770 Mean \pm SD; n = 4. The significance is relative to clone 635. **i.** mRNA expression levels of the indicated
771 genes in the indicated SK-LMS-1 clones. Mean \pm SD; n = 4. The significance is relative to clone 635. **j-k.**
772 Detailed view of the H3K27ac (green) and H3K27me3 (light-blue) tracks at the *IL1B* (j) and *CDKN1A* (k)
773 loci in SK-LMS-1/*HDAC4^{+/+}* and *-/-*, as indicated. Red boxes highlight the H3K27ac regions significantly
774 hyper-acetylated in *HDAC4^{-/-}*, that correspond to a super-enhancer in the case of *IL1B* (SE_02_17300084)
775 and to an intronic region previously associated to class IIa HDACs binding for *CDKN1A*. In the latter case a
776 strong demethylation in *HDAC4^{-/-}* affects the whole locus.

777 **Figure 3. Time-course morphological and transcriptional alteration induced by HDAC4 depletion. a.**
778 Immunoblot analysis of LMNB1, γ H2AX and H1.2-GFP in SK-LMS-1/*HDAC4^{-/-}* cells re-expressing
779 *HDAC4^{PAM}-ER*. Cells were harvested at the indicated time after 4-OHT removal. SMC3 was used as loading
780 control. **b.** mRNA expression levels of the indicated genes. Mean \pm SD; n = 4. **c.** Representative images of
781 the combination of cellular phenotypes observed after the depletion of HDAC4 in SK-LMS-1 cells (scale bar
782 10 μ m). **d.** Quantification of the time-course accumulation of the phenotypes represented in Fig. 3C in the
783 indicated cells. Mean \pm SD; n = 5. At least 200 individual cells were evaluated in each biological replicate.

784 **Figure 4. HDAC4 depletion causes the rapid accumulation of TP53BP1 foci and bodies in G2 and the**
785 **subsequent mitotic slowdown and impairment.** Heatmap representing the quantification of the TP53BP1
786 foci/bodies in SK-LMS-1/*HDAC4^{-/-}*/*HDAC4^{PAM}-ER*, during 74h of analysis starting from 6h after 4-OHT
787 removal (time “0”), as indicated. The intensity of the red is proportional to the number of TP53BP1 spots. 10
788 and 9 starting cells were analyzed respectively for the +4-OHT and the -4-OHT conditions.

789 **Figure 5. LMNB1 re-expression and hypoxic growing conditions have minimal and complementary**
790 **effects on the senescence induced by HDAC4 loss in SK-LMS-1 cells. a.** Analysis of the % of SK-LMS-
791 1/*HDAC4*^{-/-} cells, grown in normoxia, expressing H1.2-GFP or GFP-LMNB1, as indicated, and re-expressing
792 (+4-OHT) or not (-4-OHT) *HDAC4*^{PAM}-ER, displaying positivity for SA-β-gal or the accumulation of CCFs
793 and naked CCFs. Mean ± SD; n = 4. The significance is relative to H1.2-GFP re-expressing cells. **b.**
794 Representative confocal picture of SK-LMS-1/*HDAC4*^{-/-} cells, expressing GFP-LMNB1 and immunostained
795 for DNA (Hoechst, blue), LMNA (red) and γH2AX (violet). Arrows point to naked CCFs, arrowheads to
796 LMNB1+ CCFs. **c-d.** Immunoblot analysis of HIF-1α, γH2AX, GFP-LMNB1 and H1.2-GFP (anti-GFP
797 antibody) in SK-LMS-1/*HDAC4*^{-/-} cells, re-expressing (+4-OHT) or not (-4-OHT) *HDAC4*^{PAM}-ER and
798 expressing the indicated transgenes. Lysates were generated after 4d of culture in normoxia or in hypoxia, as
799 indicated. **e.** Analysis of the SA-β-gal positivity in the cells described in Fig. 5D. The significance is relative
800 to the same cells grown in normoxia. Mean ± SD; n = 3. **f.** mRNA expression levels of the indicated genes in
801 SK-LMS-1 cells generated and maintained as described in Fig. 5D. The levels are relative to wt cells grown
802 in normoxia (considered as 1). The significance is relative to SK-LMS-1/*HDAC4*^{-/-} cells grown in normoxia.
803 Mean ± SD; n = 3.

804 **Figure 6. HDAC4 depletion causes the accumulation of replication stress and of cytoplasmic dsRNAs**
805 **of retroviral origin. a.** Immunoblot analysis in SK-LMS-1/*HDAC4*^{-/-} cells re-expressing *HDAC4*^{PAM}-ER.
806 Cells were harvested at the indicated time after 4-OHT wash out. Actin was used as loading control. **b.**
807 Immunoblot analysis in SK-LMS-1/*HDAC4*^{-/-} cells re-expressing *HDAC4*^{PAM}-ER. 4-OHT was removed 6h
808 before the treatment with CDK4i (1μM), as indicated. Actin was used as loading control. **c.** Analysis of
809 BrdU, SA-β-gal, TP53BP1 foci and γH2AX positivity in the indicated cells treated as in Fig. 6B. Mean ±
810 SD; n = 4. The significance is relative to untreated cells. **d-e.** Time-course immunoblot analysis in SK-LMS-
811 1/*HDAC4*^{-/-} cells re-expressing or not *HDAC4*^{PAM}-ER (48h) and treated for the indicated time with 500nM
812 Aphidicolin (APH) or 3.125μM Camptothecin (CPT). Actin was used as loading control. Densitometric
813 analysis of γH2AX/Actin ratio is provided. **f.** Immunoblot analysis on the same cells described in Fig. 6D,
814 harvested at the indicated time after the release from 1h APH treatment. Densitometric analysis of
815 γH2AX/Actin ratio is provided. **g.** Histogram representing the percentage of hyper-acetylated (green bar) or
816 demethylated (light blue) H3K27 peaks in SK-LMS-1/*HDAC4*^{-/-} cells and falling in the indicated genomic
817 elements or displaying the indicated epigenomic features. The genome coverage of each element is indicated
818 by gray bars. **h.** Histogram representing the enrichment of each element described in Fig. 6g in respect to the
819 expected distribution calculated according to the genome coverage. **i.** Histogram of 10 CFSs associated to the
820 transcripts (median of the associated transcripts, indicated as RNA (KO/wt)) more up-regulated (red) or
821 down-regulated (blue) in SK-LMS-1/*HDAC4*^{-/-} in respect to *HDAC4*^{+/+} cells. The correlation between the
822 RNA (KO/wt) and H3K27ac/me3 levels and the gene length are indicated. **j.** Histogram representing the
823 RNA levels of the indicated genes/ERVs in SK-LMS-1/*HDAC4*^{-/-}/*HDAC4*^{PAM}-ER cells, at 72h from last 4-
824 OHT treatment (+4-OHT) or wash-out (-4-OHT). Mean ± SD; n = 4. The significance is relative to wt cells.

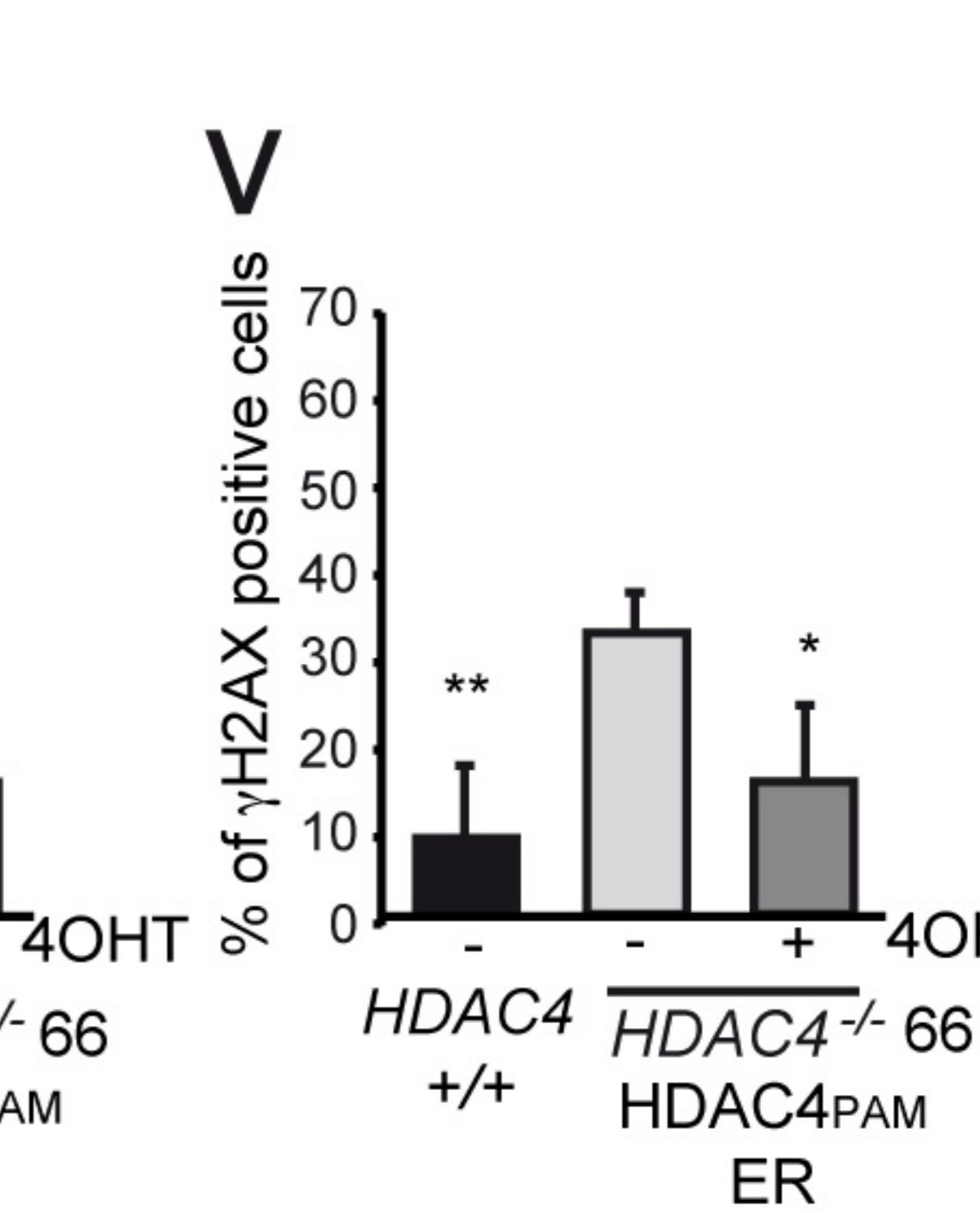
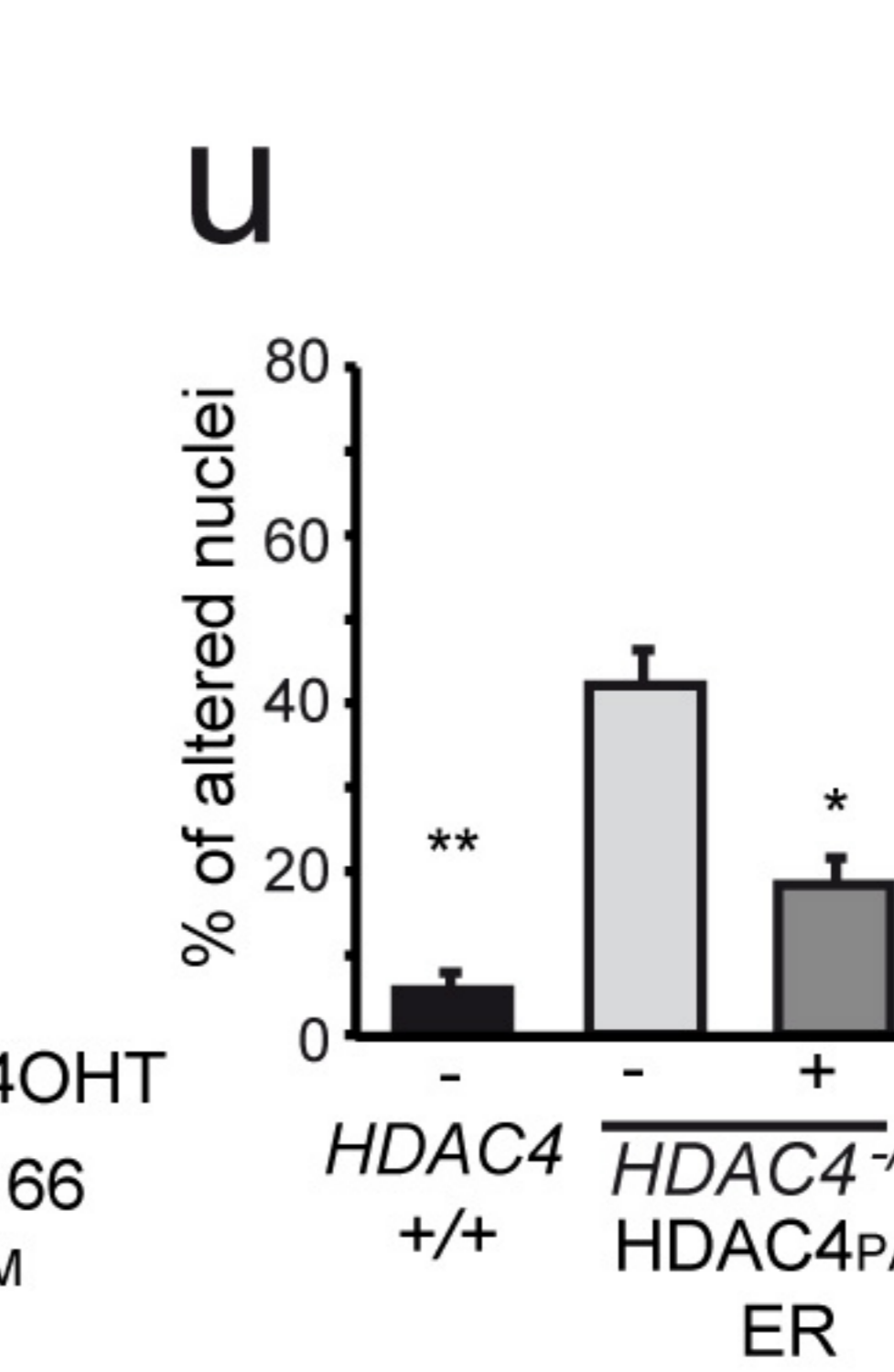
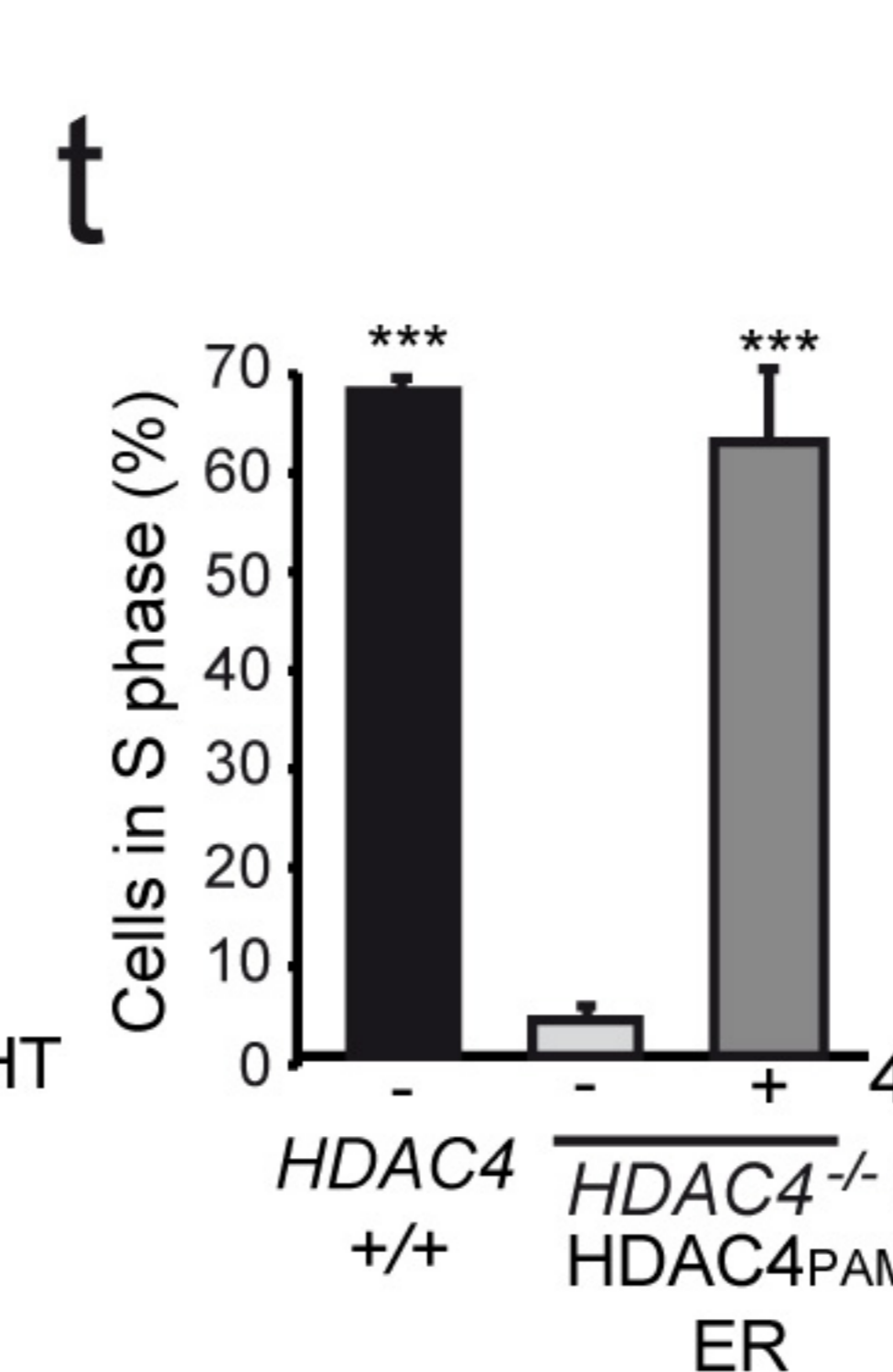
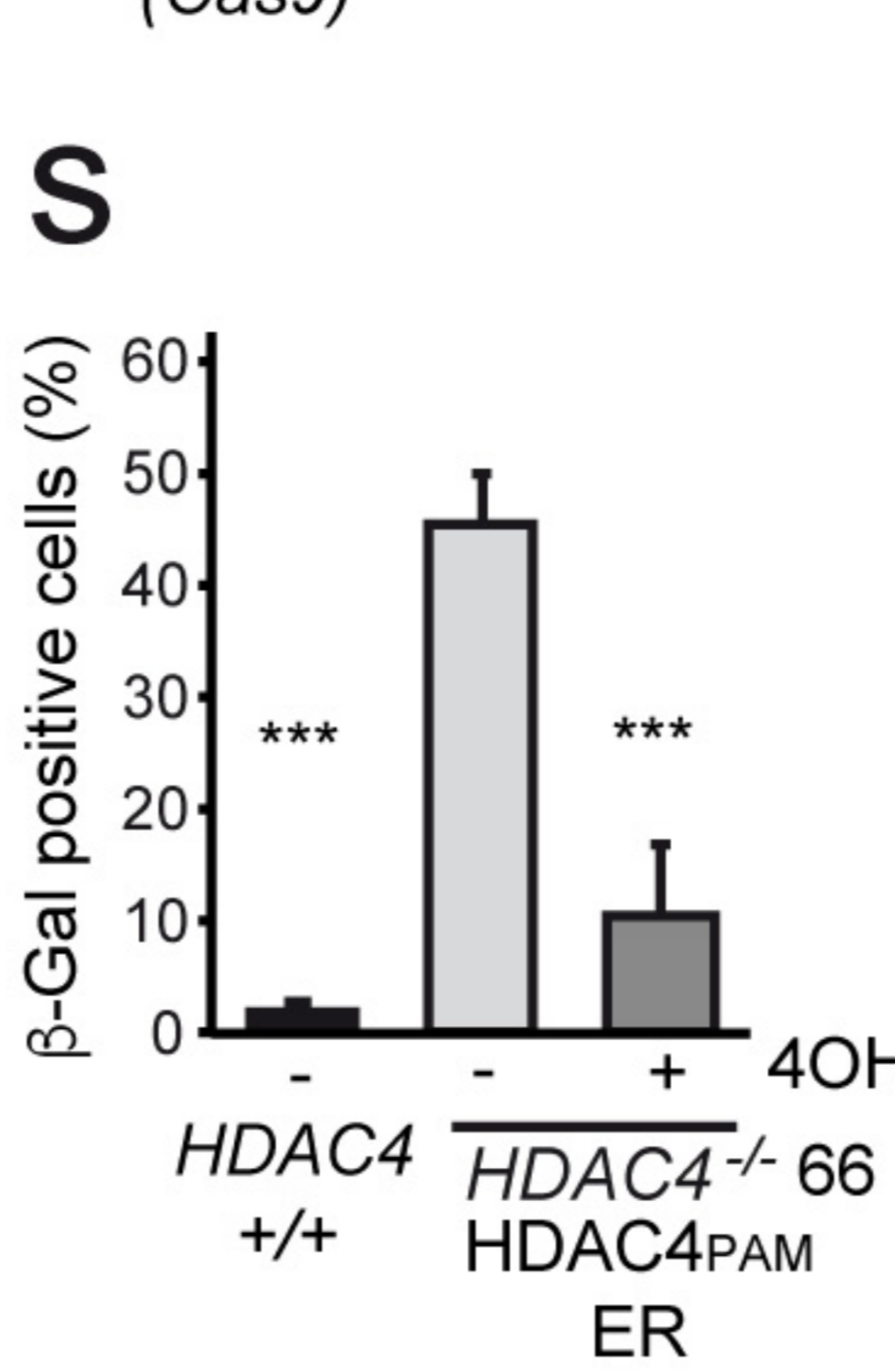
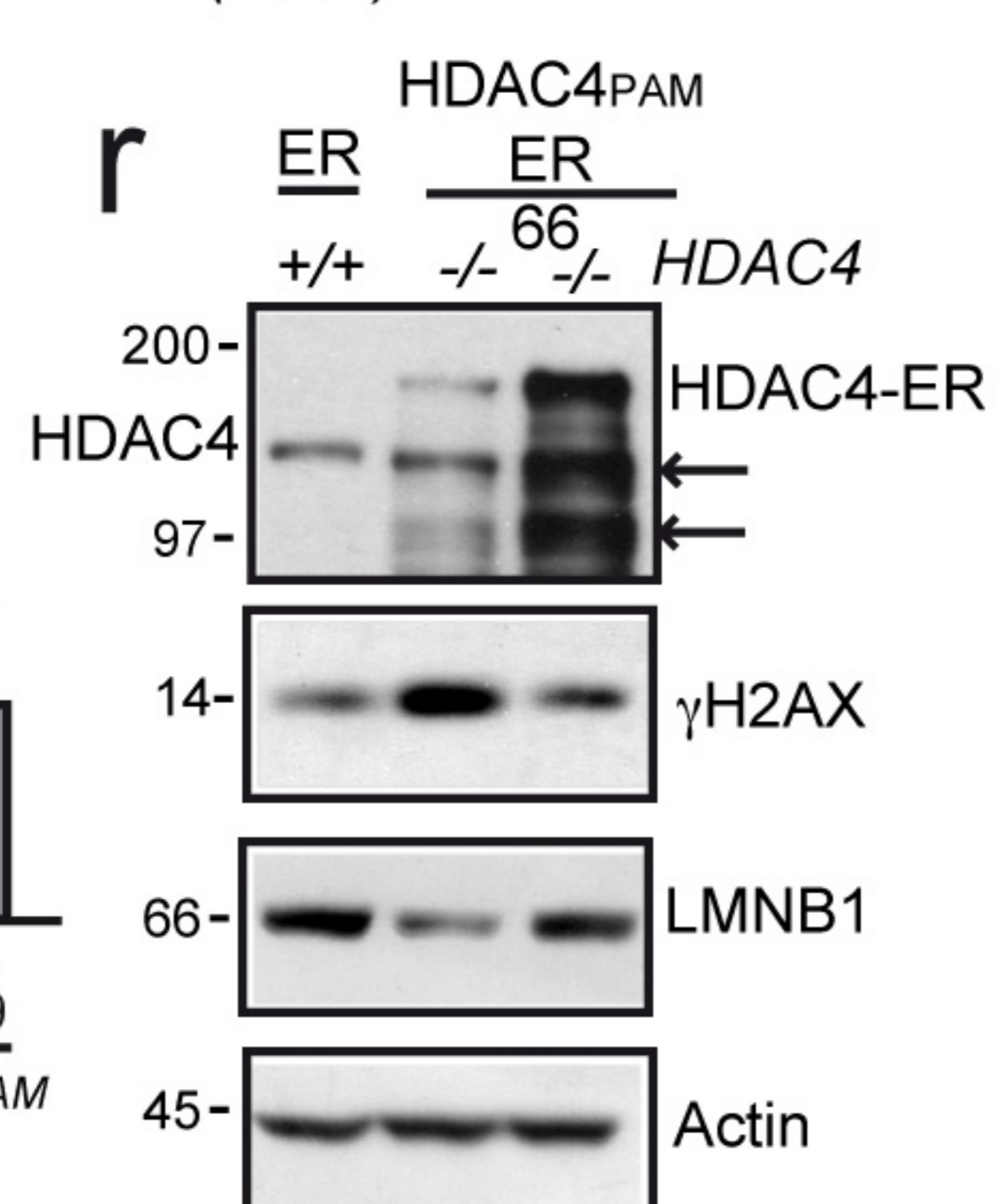
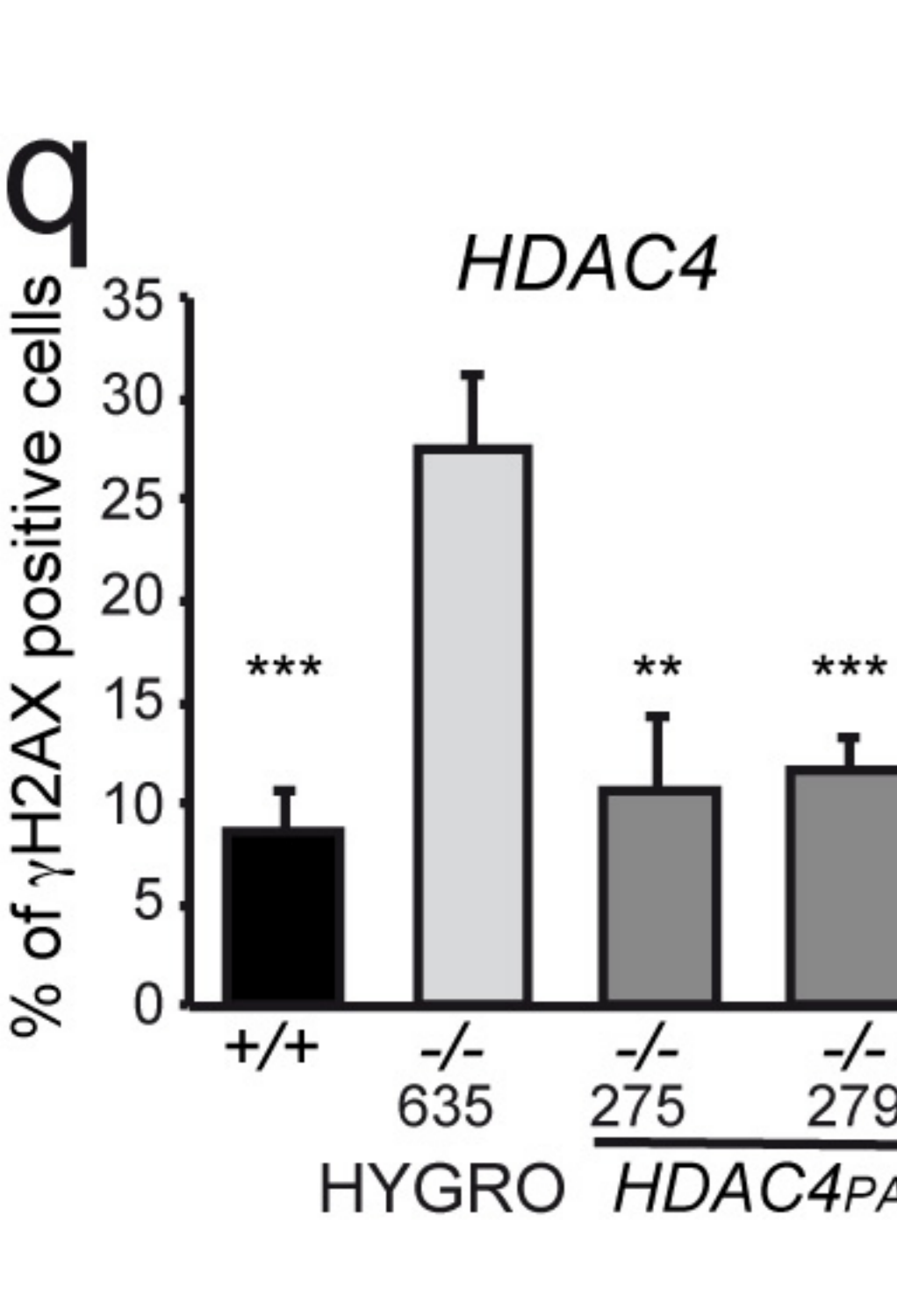
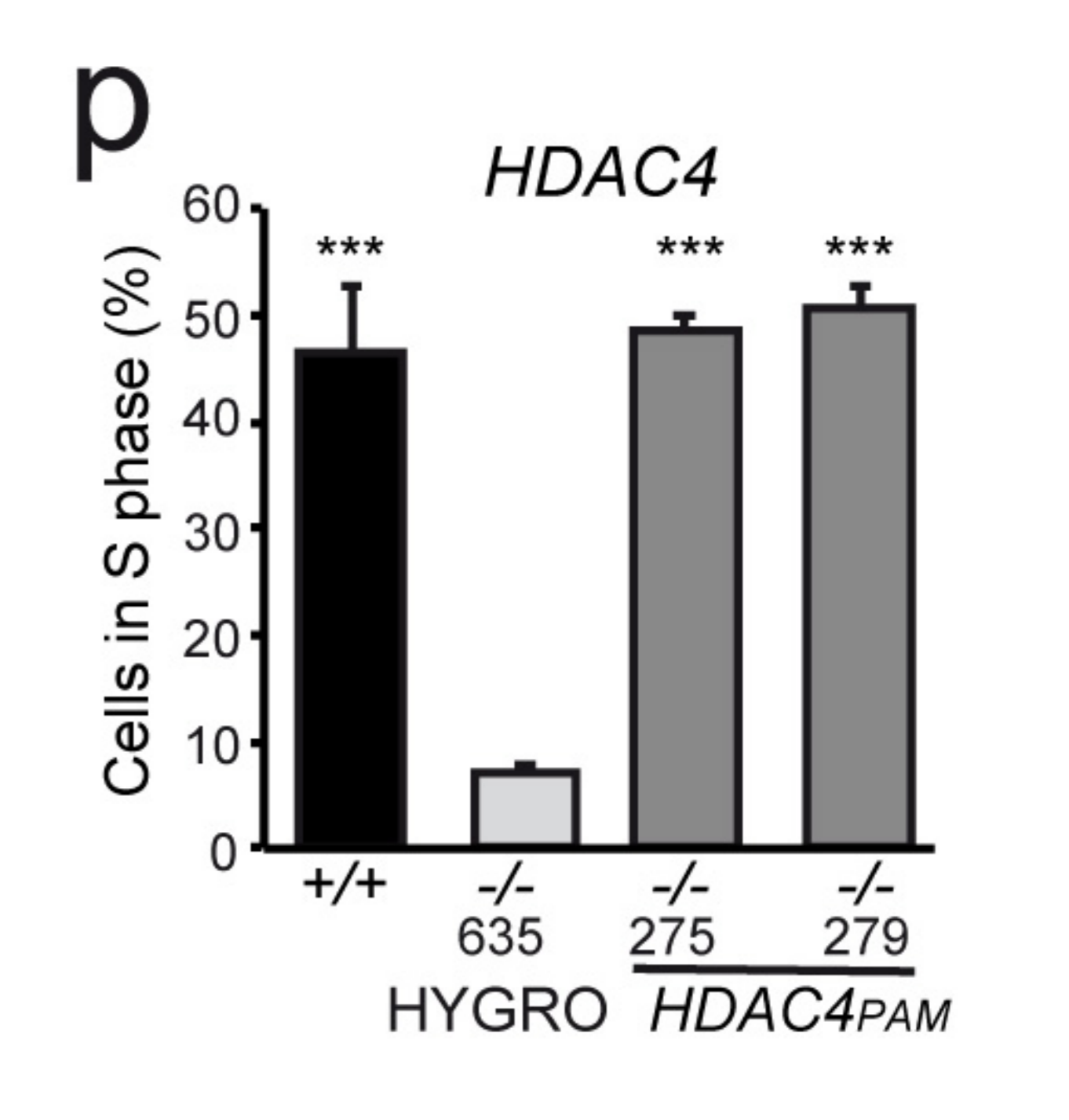
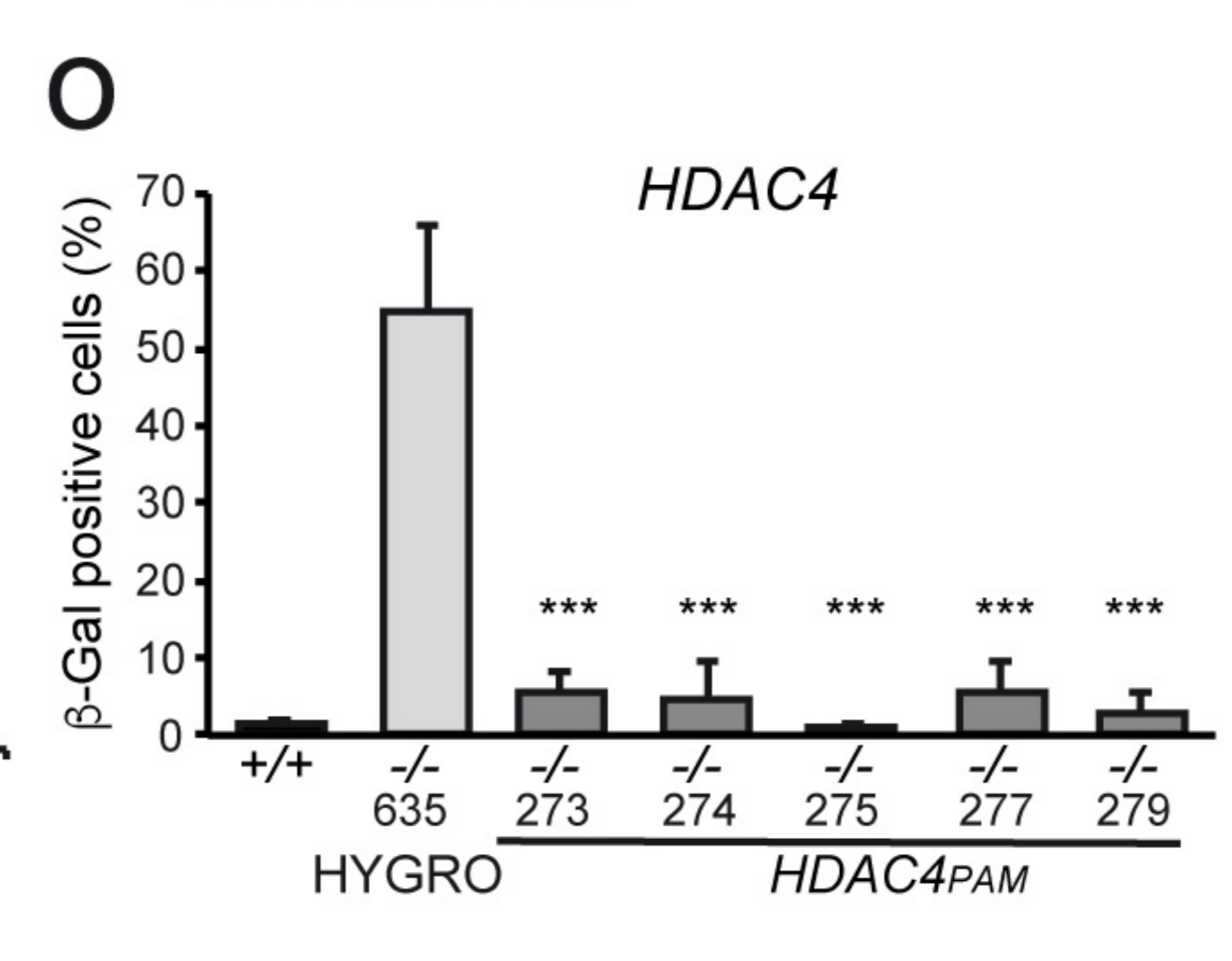
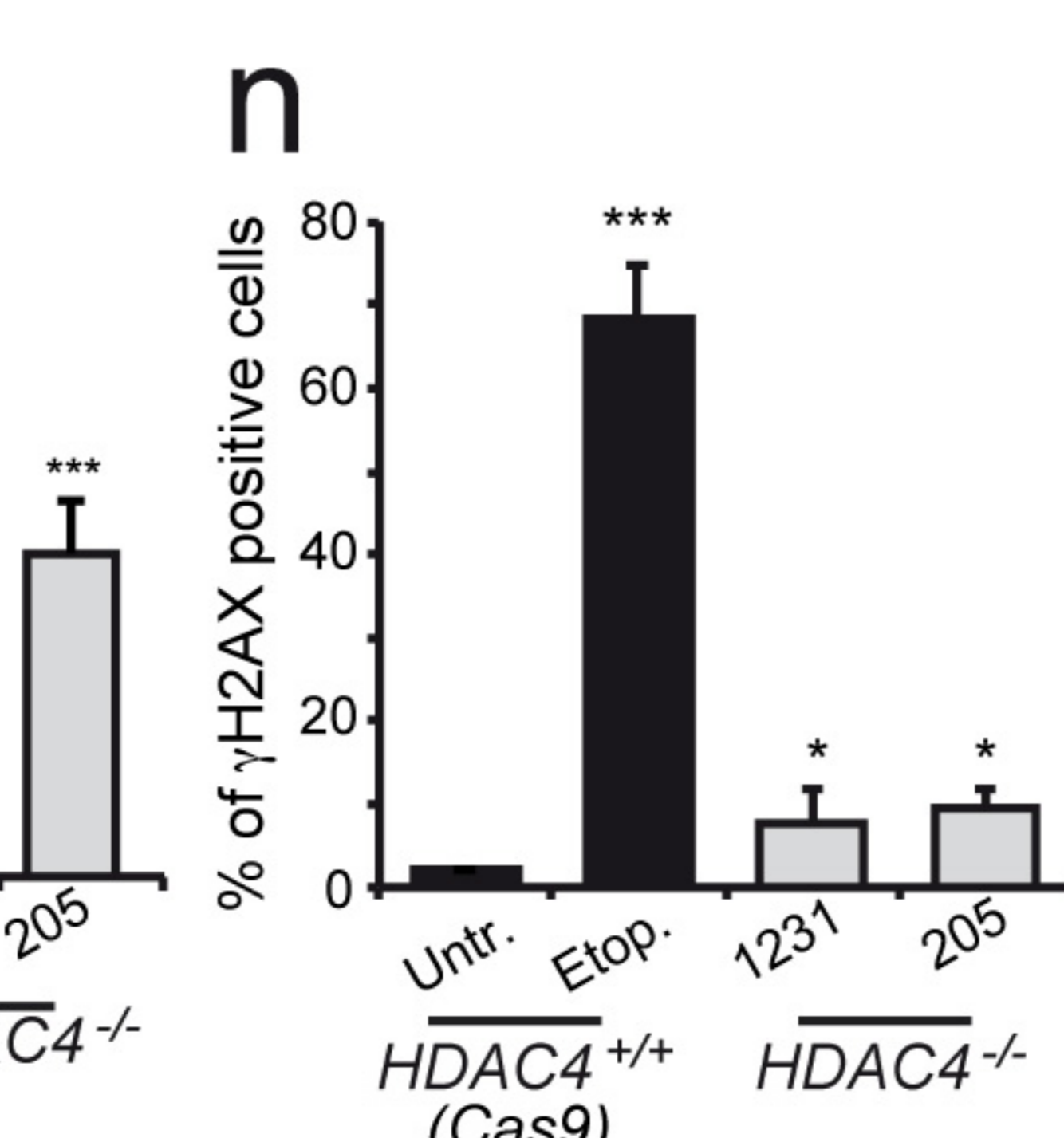
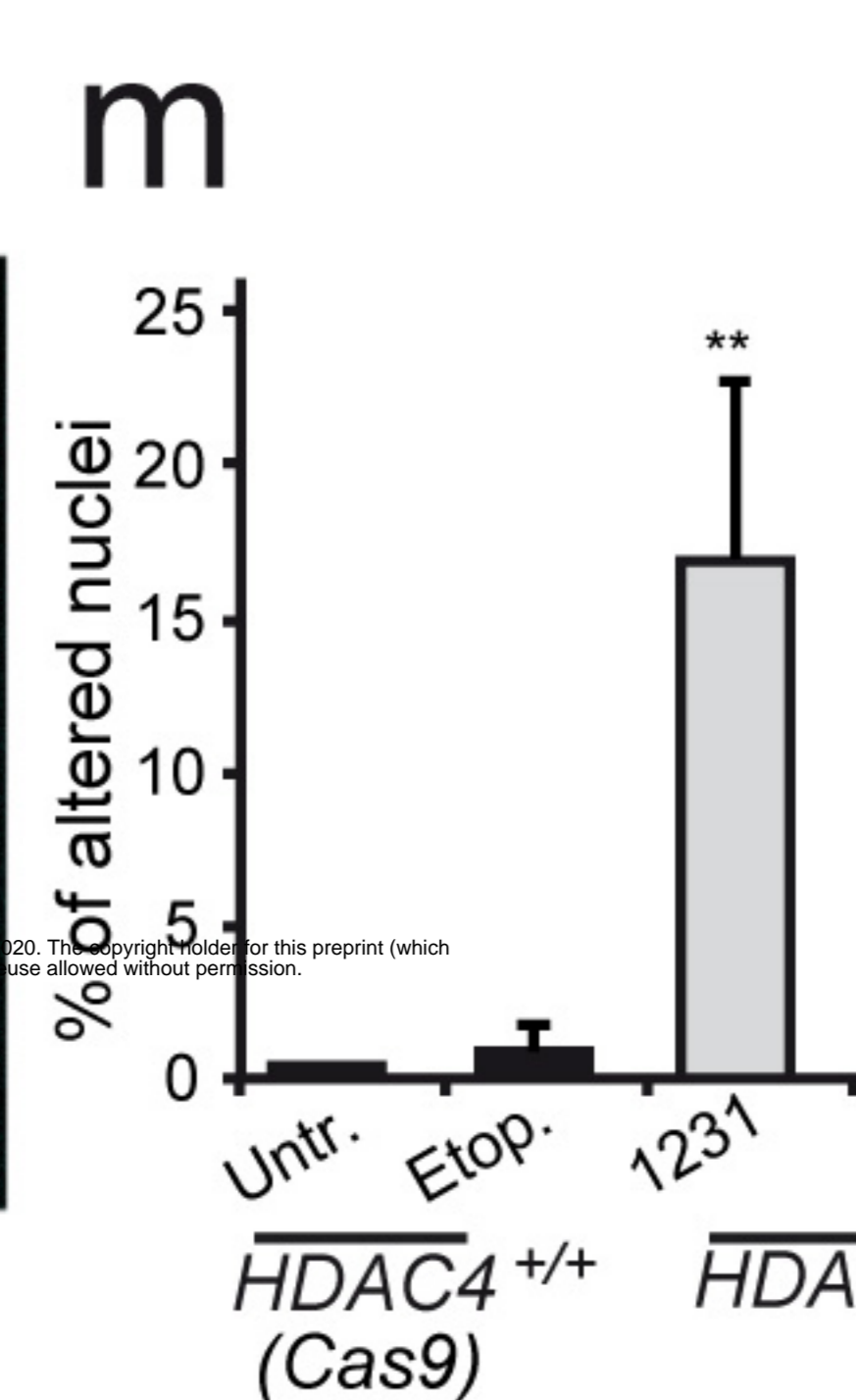
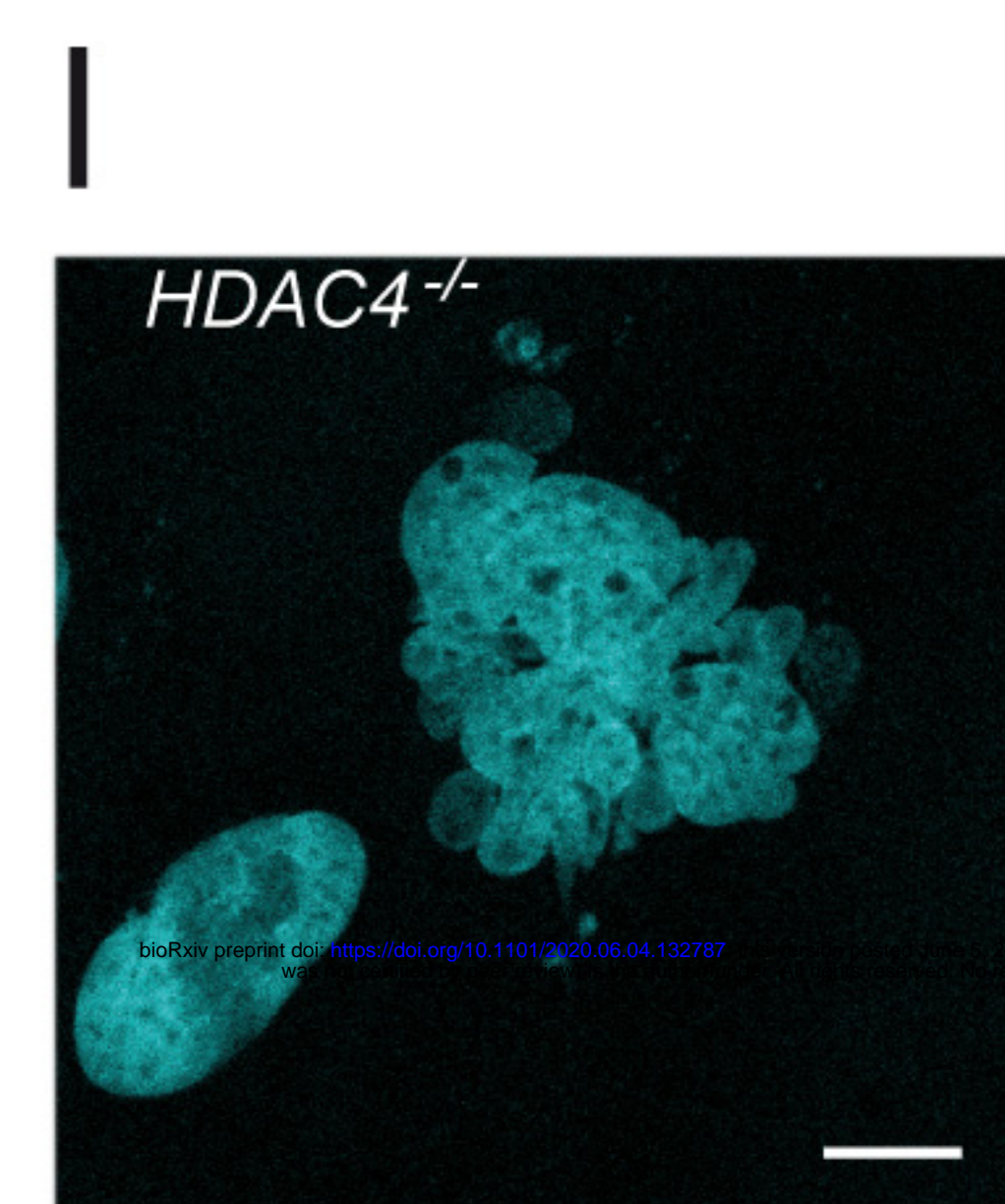
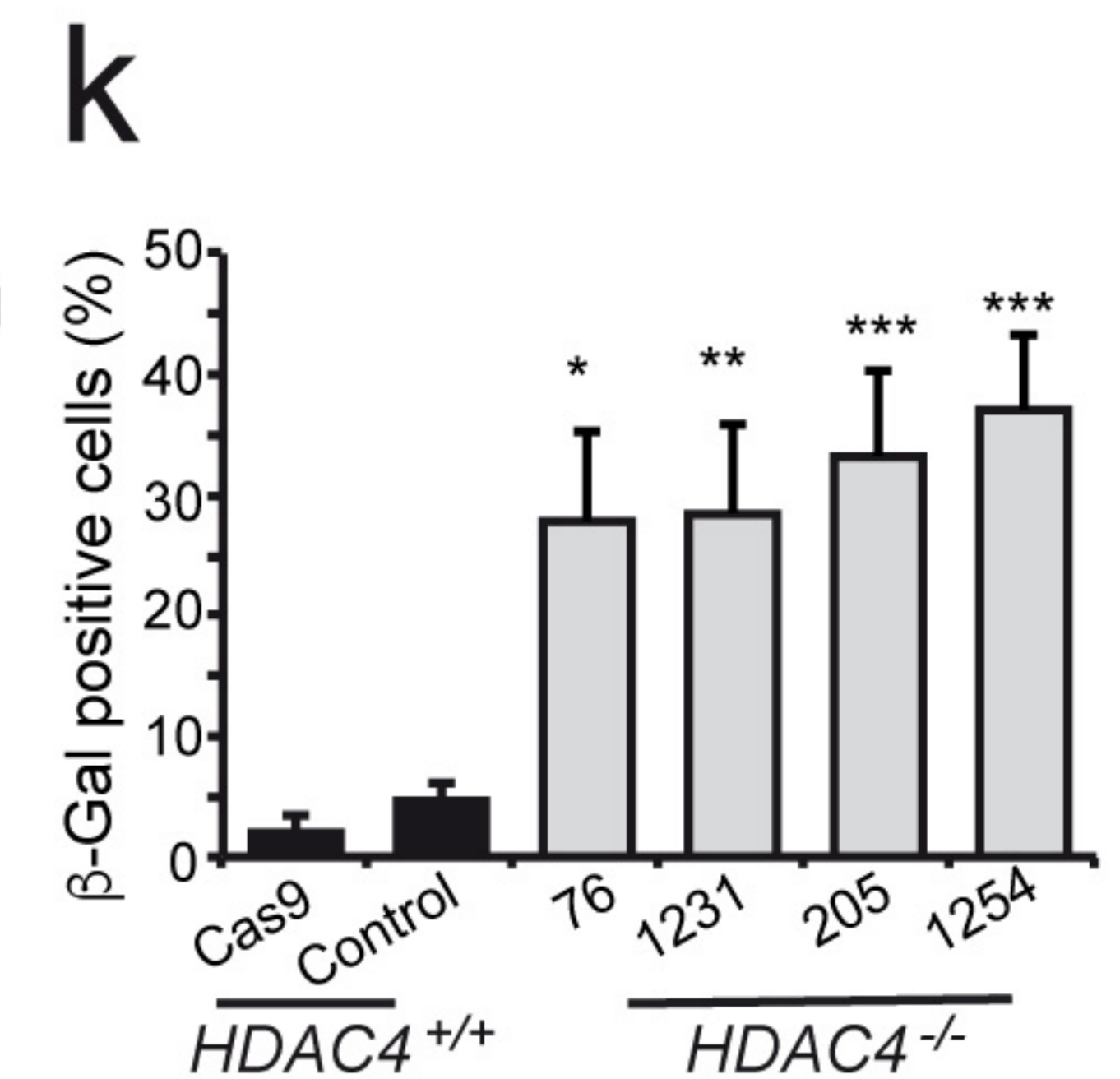
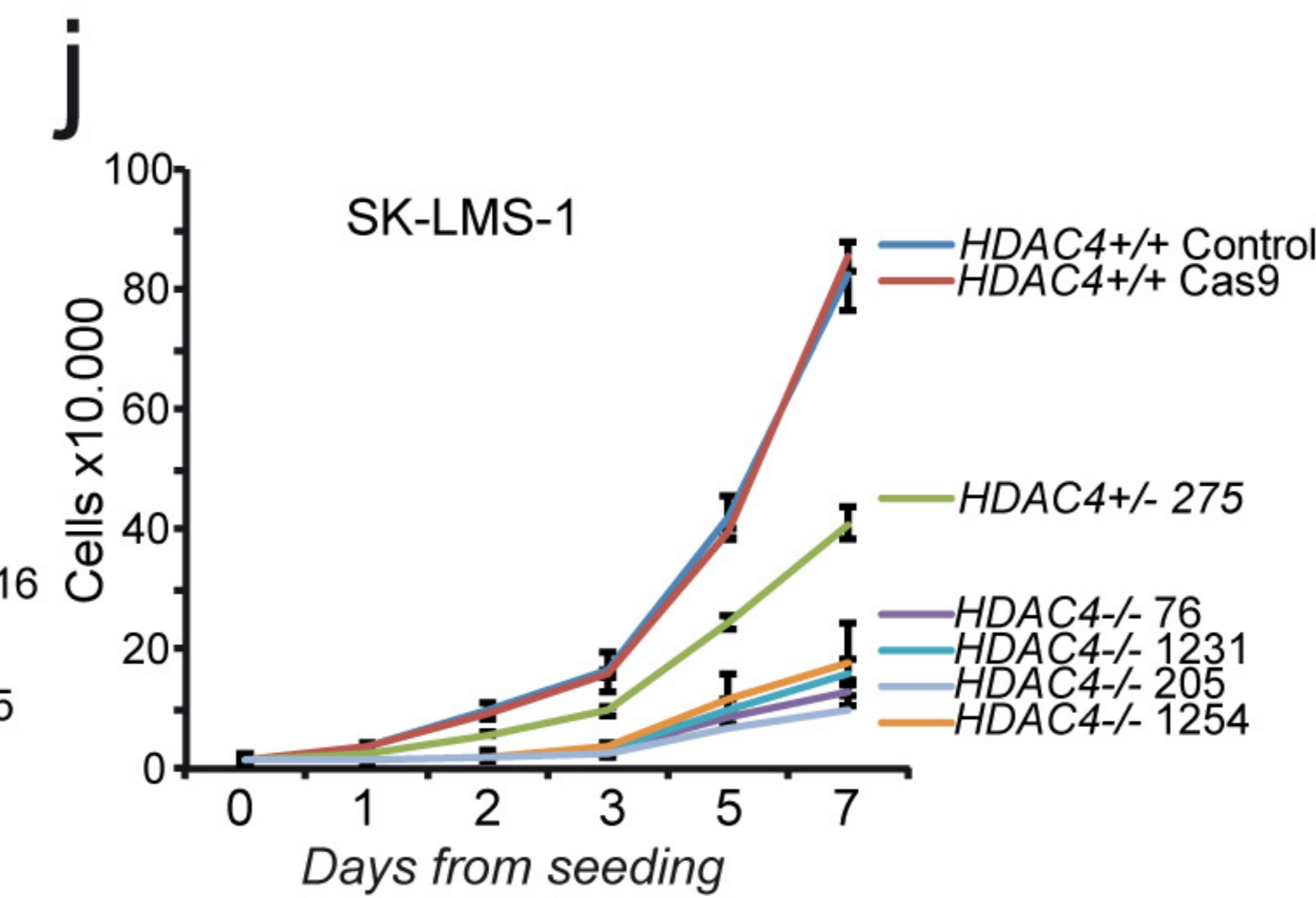
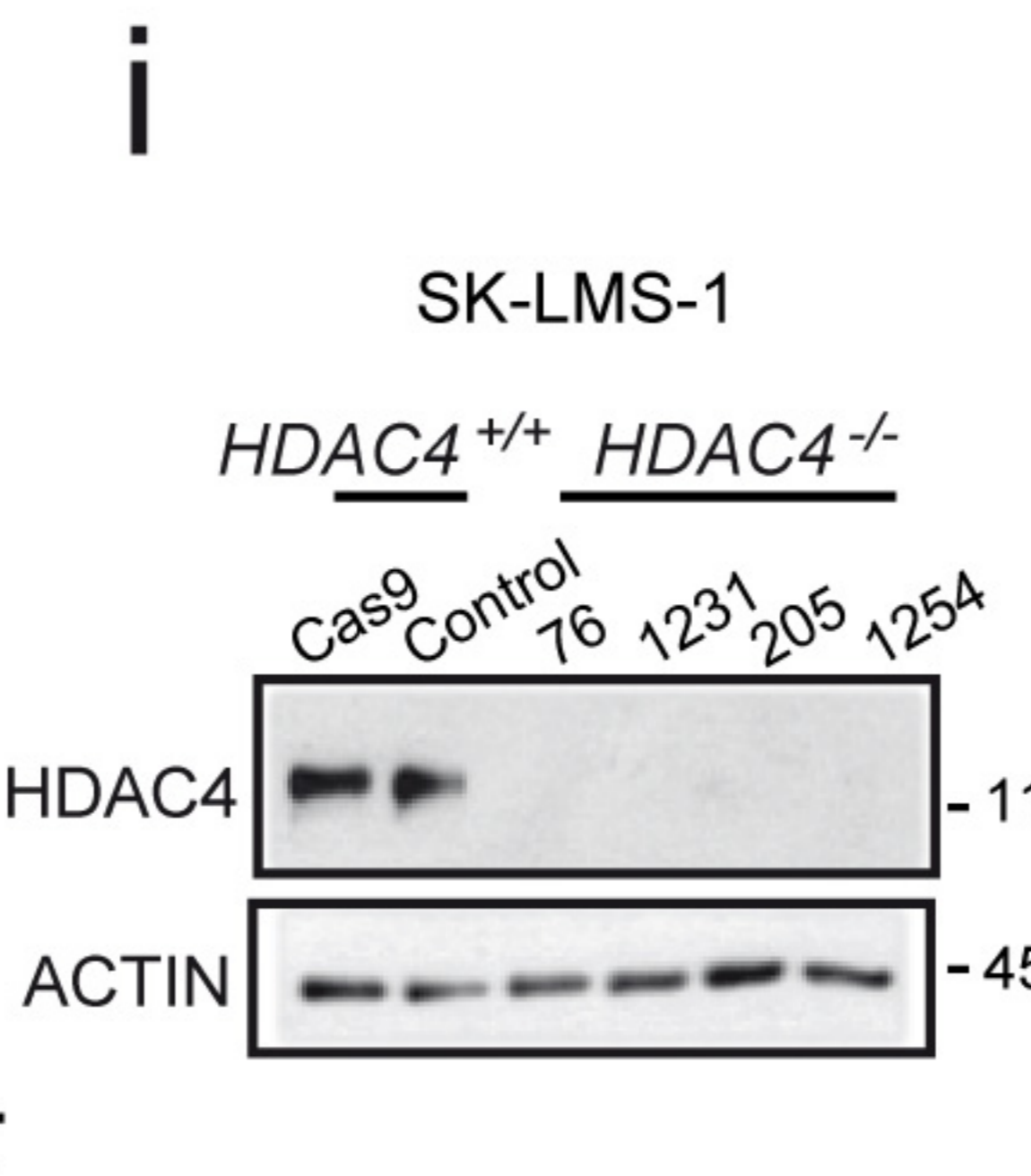
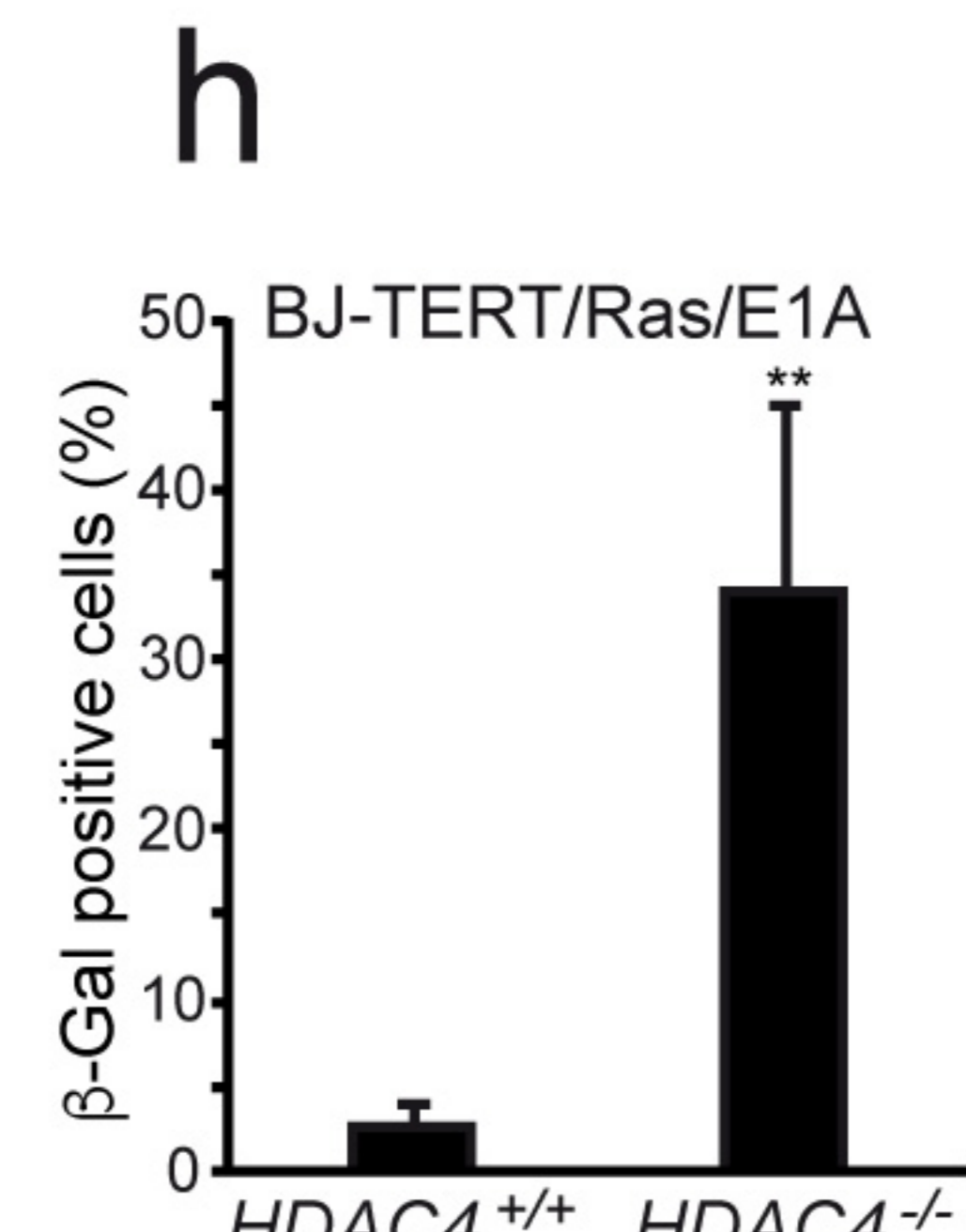
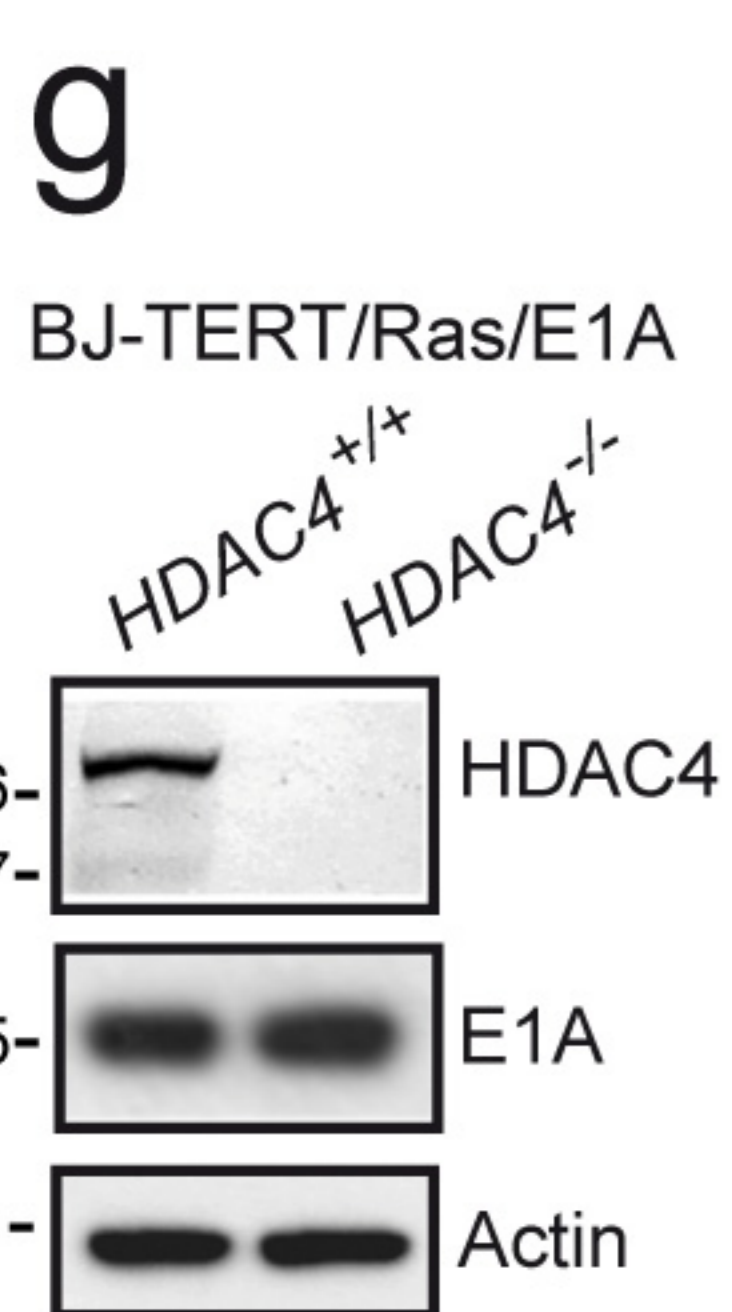
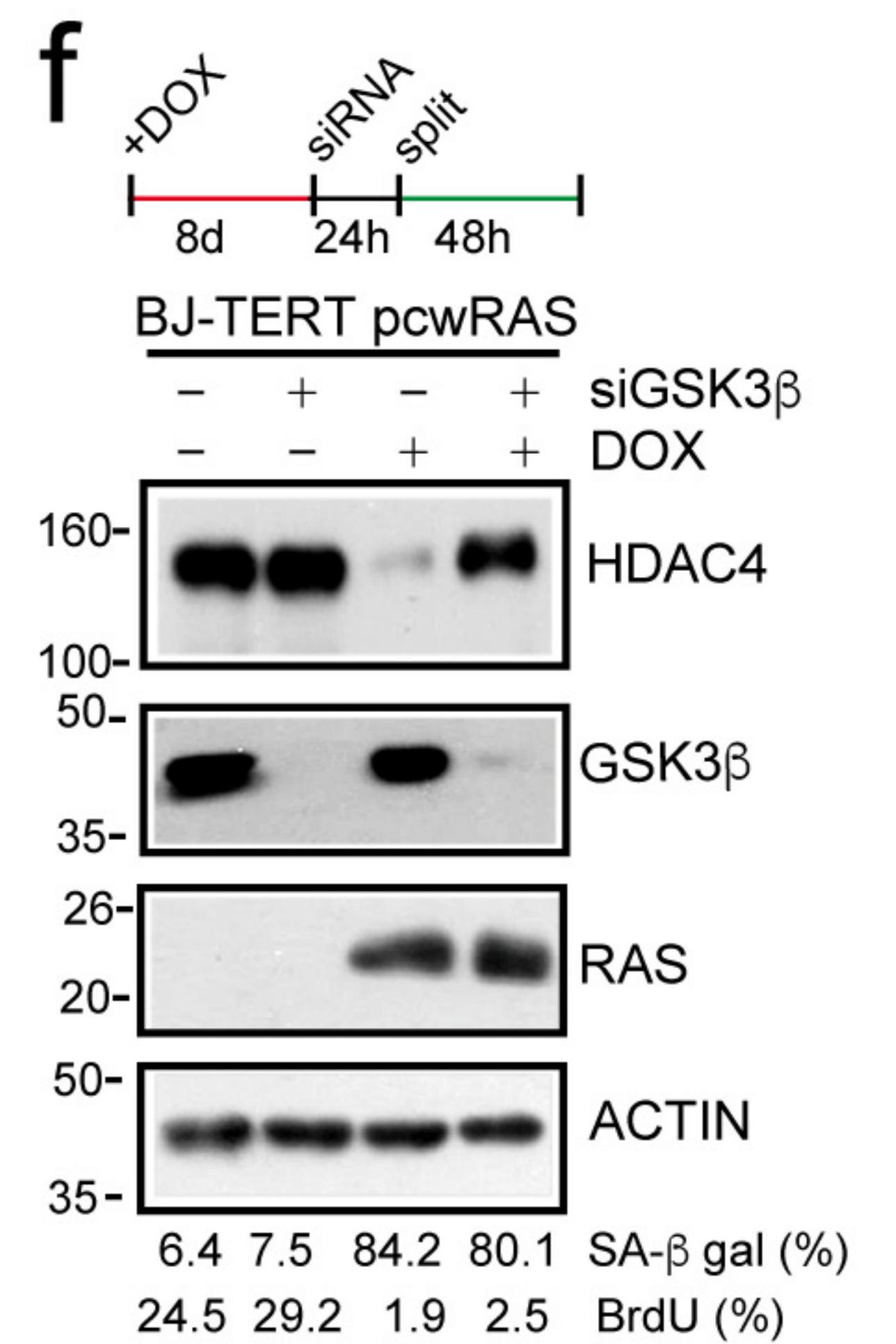
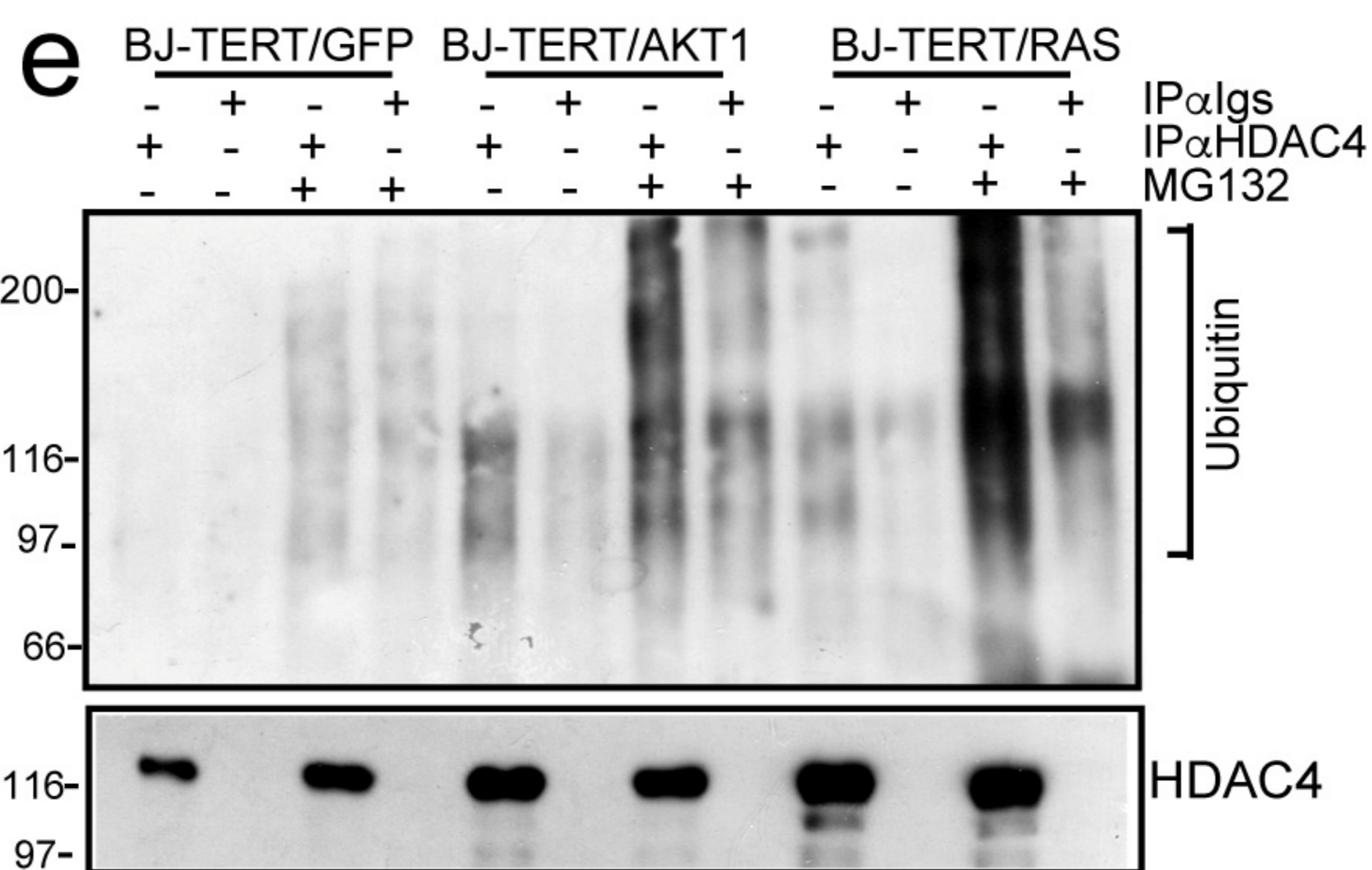
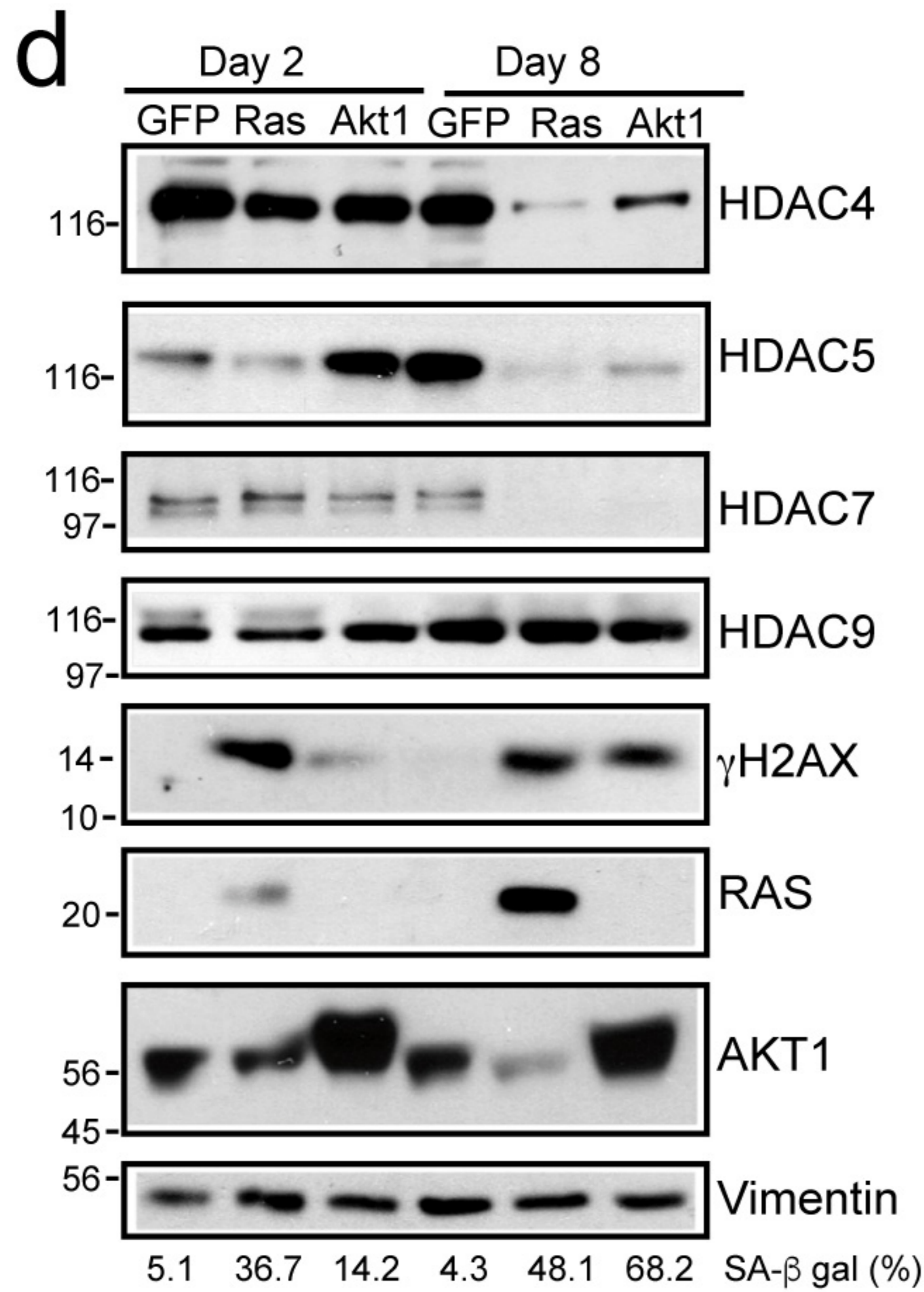
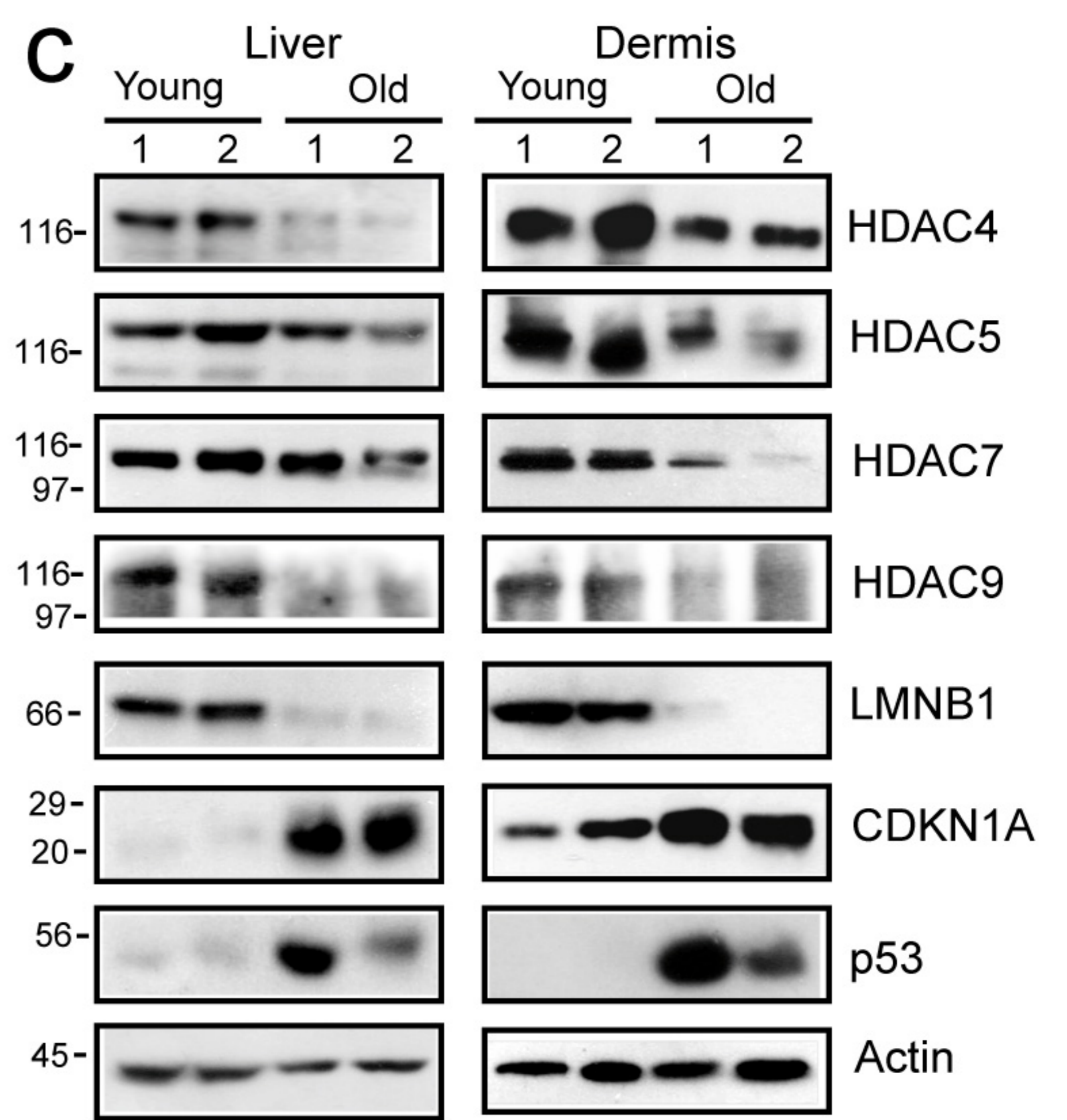
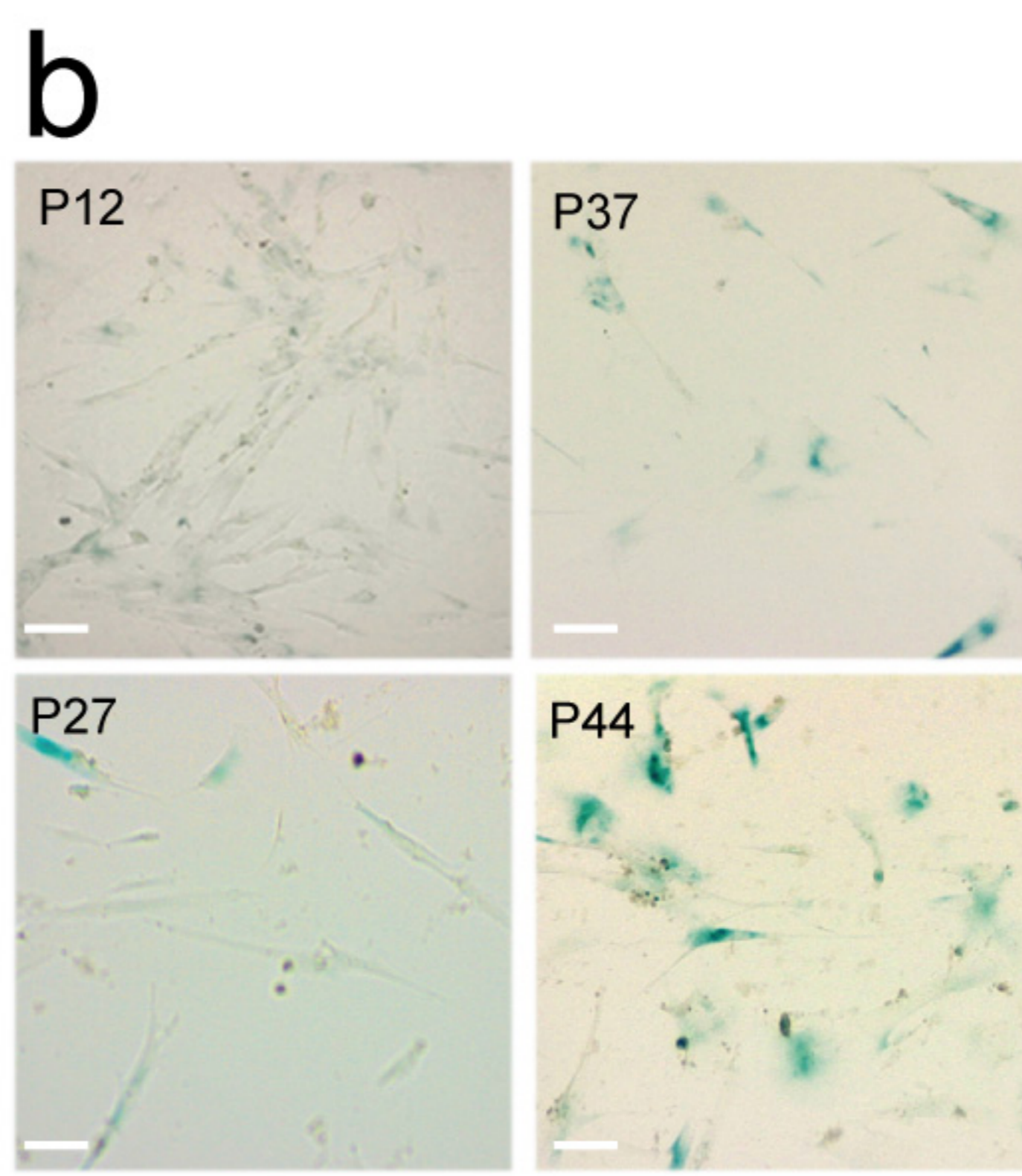
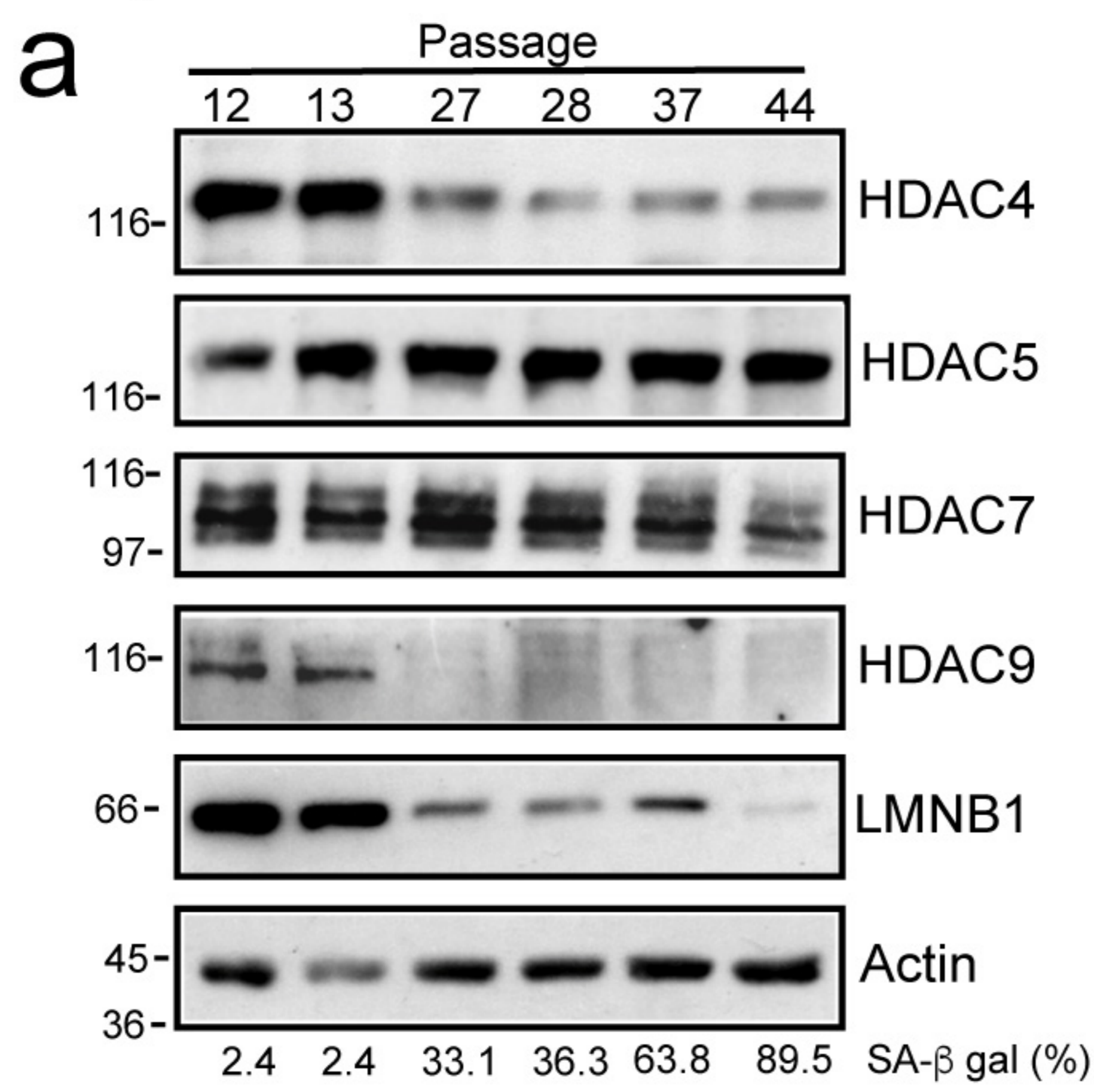
825 **k.** Representative confocal pictures of the indicated SK-LMS-1 cells at 48h from 4-OHT removal/addition.
826 Immunofluorescence was performed to visualize dsRNAs (red) and nuclei (blue). Scale bar 10 μ M.

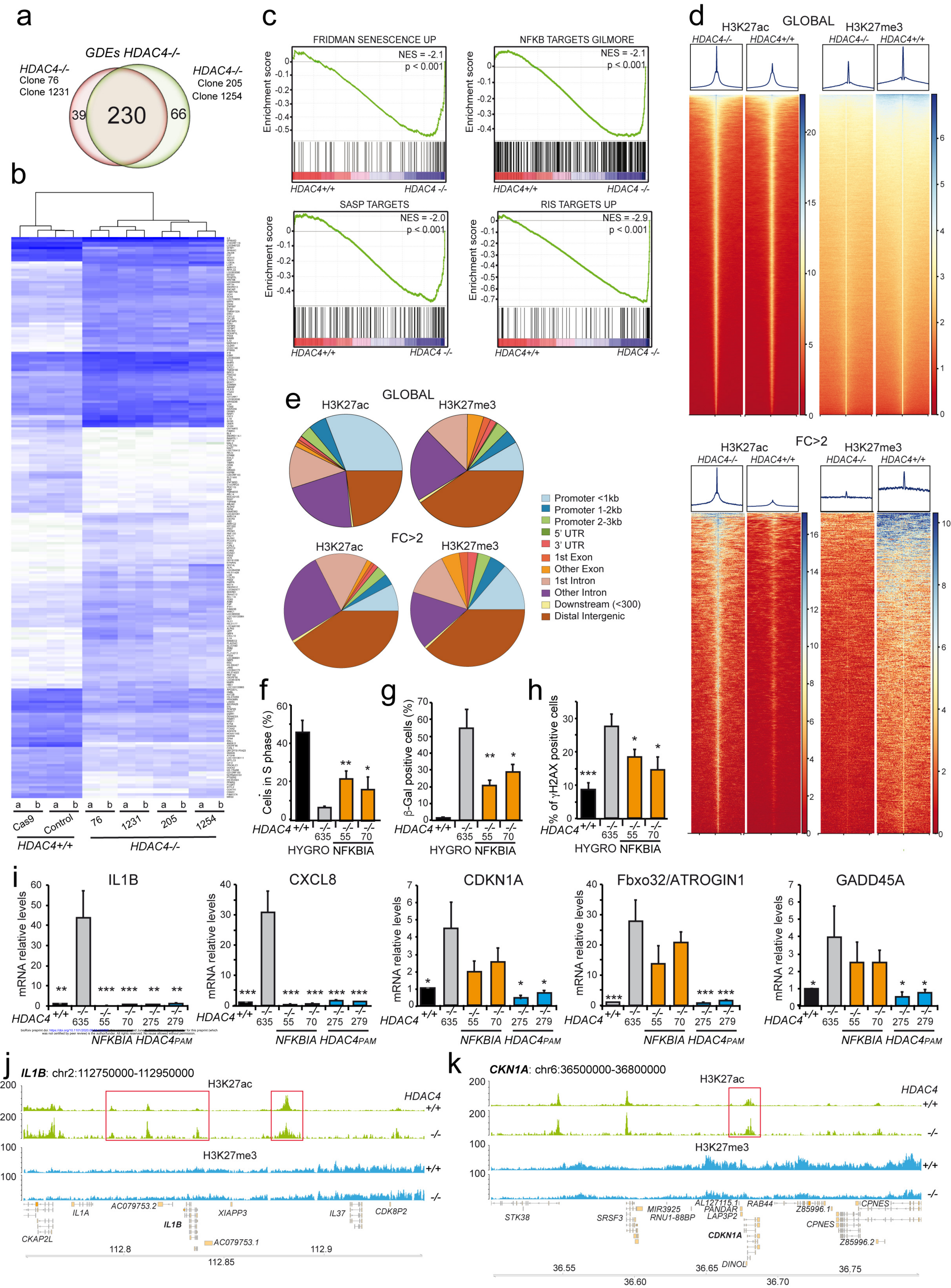
827 **Figure 7. The epigenetic stress induced by HDAC4 depletion causes the accumulation of ERVs and**
828 **triggers the IFN-response. a-b.** mRNA expression levels of the indicated genes, in SK-LMS-1/*HDAC4*^{-/-}
829 /*HDAC4*^{PAM}-*ER* re-expressing cells harvested at the indicated time after HDAC4 depletion (a) and in IMR90
830 cells harvested at the indicated cellular splittings (b). Mean \pm SD; n = 3. The significance is relative to time 0
831 (a) or to split 12 (b). **c.** Quantification of the enrichment over input of the indicated species of RNAs in the
832 preparation of dsRNAs used to treat the cells in Fig. 7d/e. **d-e.** Analysis of SA- β -gal (c) and Trypan blue (d)
833 positivity in SK-LMS-1 cells transfected for 72h with 30pmoles of double-stranded enriched RNAs obtained
834 from *HDAC4*^{-/-} cells, and pre-digested or not for 30' with 50u RNaseIII. **f.** Heat-map of the top (1%)
835 H3K27ac and H3K27me3 enriched peaks in the indicated SK-LMS-1 cells in a 30kb region around an ERV;
836 each row represents the same ERV in wt and KO cells. **g.** Histogram representing the percentage of hyper-
837 acetylated (green bar) or demethylated (light blue) H3K27 peaks in SK-LMS-1/*HDAC4*^{-/-} cells and falling in
838 ERVs. The genome coverage of each element is indicated by gray bars. **h.** Histogram representing the
839 enrichment of hyper-acetylated or demethylated ERVs as explained in Fig. 7g in respect to the expected
840 distribution calculated according to the genome coverage. **i-j.** Detailed view of H3K27ac (green) and
841 H3K27me3 (light-blue) tracks at two ERVs rich regions on Chr16 (g) and Chr17 (hH). Regions H3K27
842 hyper-acetylated (g) or demethylated (h) in SK-LMS-1/*HDAC4*^{-/-} in respect to the wt are indicated.

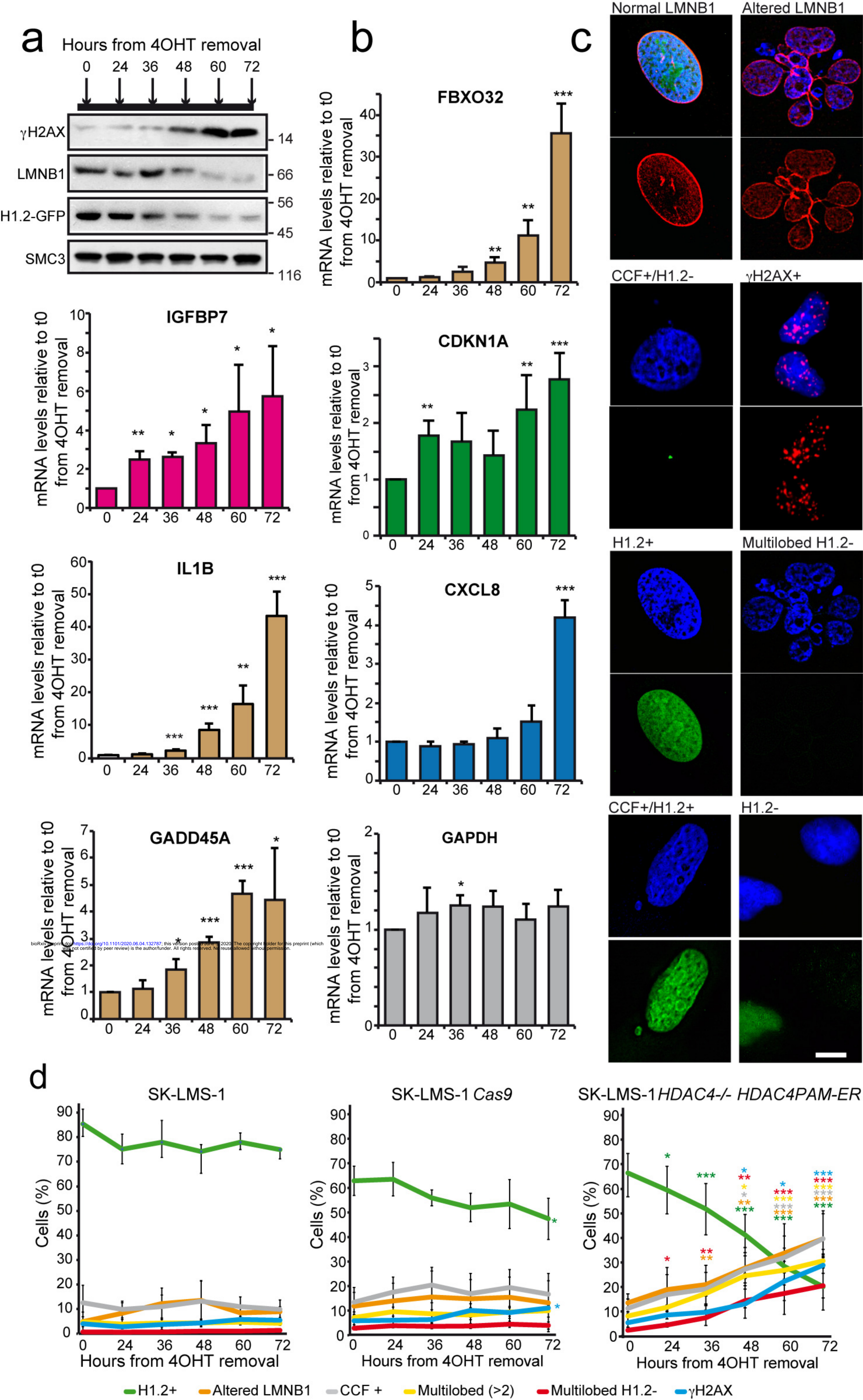
843 **Figure 8. A senescence signature triggered by the activation of RIG-1/MAVS pathway or by the**
844 **HDAC4-dependent de-repression and activation of SE sustains the premature senescence entrance. a.**
845 Microscopic images of SA- β -gal stained SK-LMS-1/*HDAC4*^{-/-} cells re-expressing HDAC4 (+4-OHT) or the
846 indicated transgenes, at 72h from HDAC4 depletion. Scale bar 50 μ m. **b.** Immunoblot analysis in the cells
847 described in Fig.8a. Densitometric analysis of γ H2AX/Actin ratio is provided. n=3. **c.** Immunoblot analysis
848 in the indicated cells treated as in fig. 6b. **d-e.** Immunoblot analysis in the indicated cells harvested after 72h
849 of HDAC4 depletion. Actin was the loading control. **f.** Analysis of SA- β positivity in wt or *HDAC4*^{-/-} SK-
850 LMS-1 cells transfected with the indicated siRNAs. Mean \pm SD; n =3. **g.** Heat-map reporting the expression
851 levels (log2 fold change relative to wt cells) of the indicated genes and ERVs in SK-LMS-1/*HDAC4*^{-/-} cells
852 expressing the indicated transgenes as described in Fig. 8b. **h.** Heat-map reporting the % of the indicated SK-
853 LMS-1 cells displaying positivity to γ H2AX, CCF, SA- β -gal and BrdU. **i.** Analysis of SA- β -gal positivity in
854 wt or *HDAC4*^{-/-} A375 cells re-expressing the indicated transgenes, 5d after HDAC4 removal. Mean \pm SD; n
855 =3. The significance is relative to *HDAC4*^{-/-}-Neo cells. **j.** Immunoblot analysis in the indicated cells
856 harvested as in Fig. 8i. SMC3 was the loading control. **k.** Heat-map reporting the expression levels (log2 fold
857 change relative to wt cells) of the indicated genes and ERVs (left) and SA- β -gal positivity (right) in the same
858 A375 cells described in fig. 8i. **l.** Heat-map reporting the expression levels (log2 fold change relative to
859 DMSO treated *HDAC4*^{PAM}-*ER* cells) of the indicated genes and ERVs, in the same SK-LMS-1 cells
860 described in fig. 6b. **m.** Histogram representing the percentage of class IIa HDACs bound peaks in the
861 indicated cells and falling in the described genomic/epigenomic elements. The genome coverage is indicated

862 by gray bars. **n.** Motif analysis of 93 HDAC4-gained SESs for putative transcription factor binding sites.
863 Motifs with $p\text{-value} < 0.5 * 10^{-4}$ were selected. **o-p.** Detailed view of 2 representative SESs directly bound by
864 HDAC4 in SK-LMS-1 wt cells in correspondence to H3K27ac-defined SEs.

865



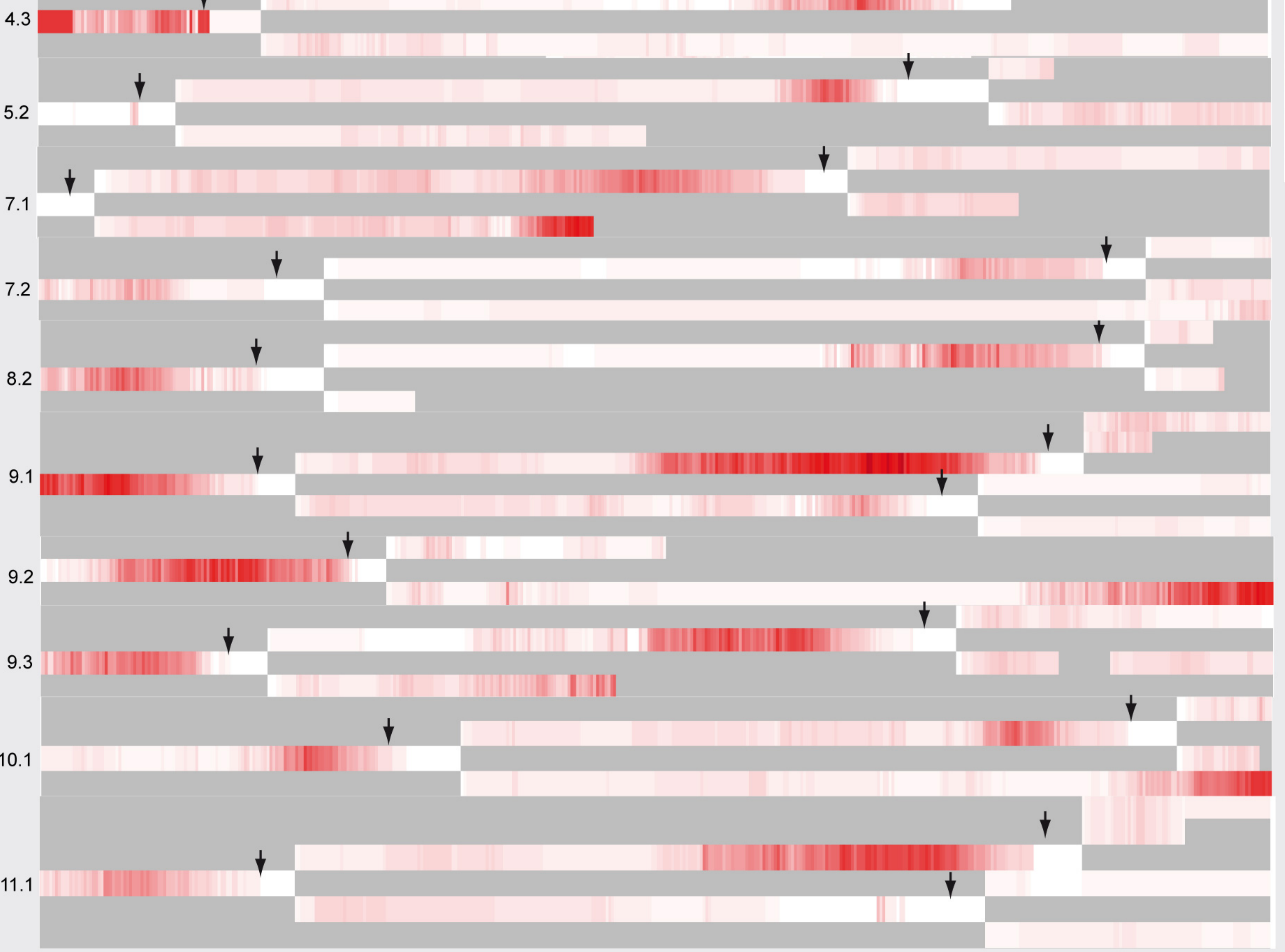
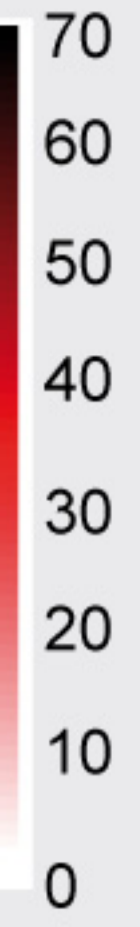




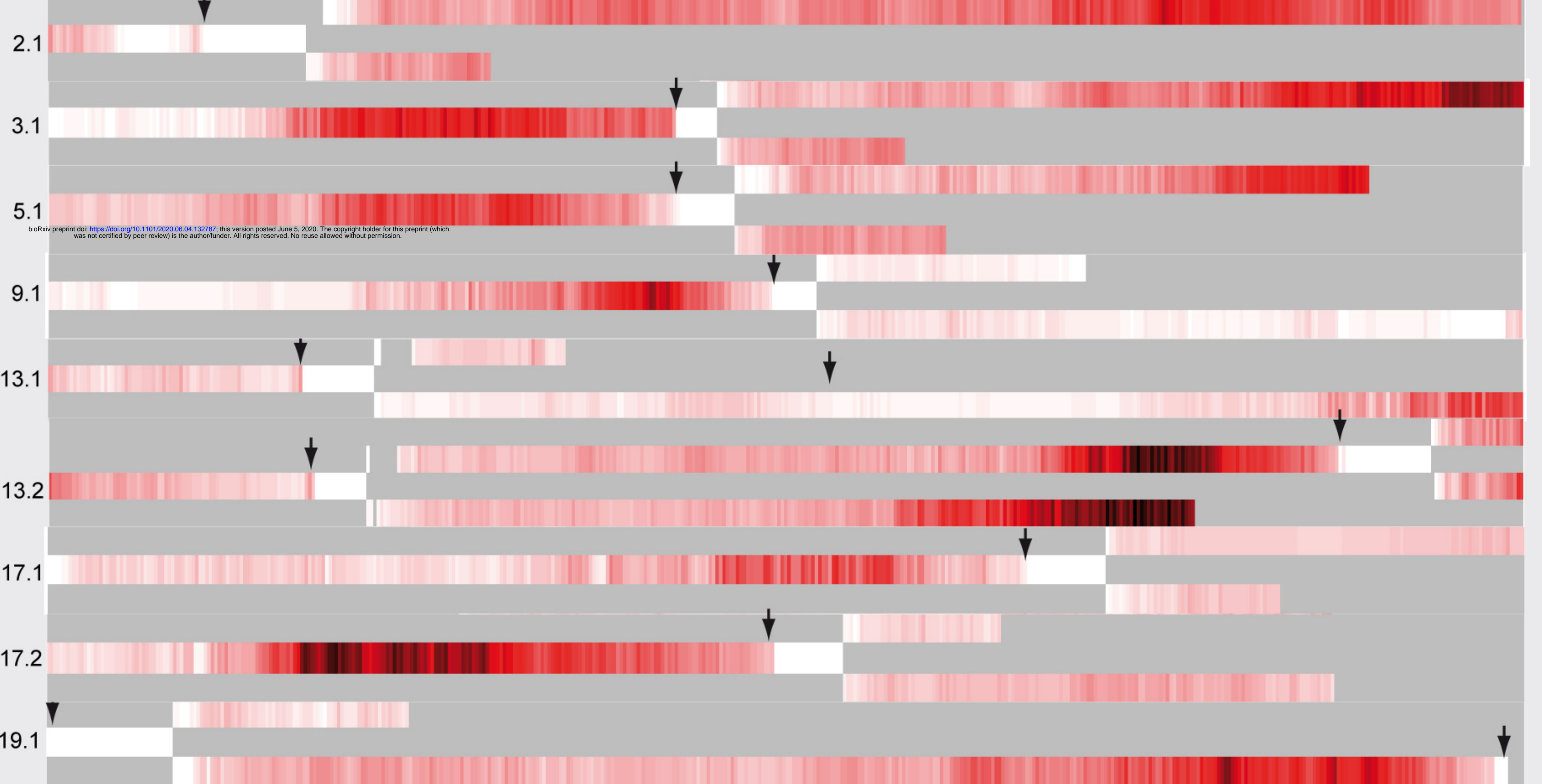
Hours

0 10 20 30 40 50 60 70 74

+ 4OHT



- 4OHT



bioRxiv preprint doi: <https://doi.org/10.1101/2020.06.04.132787>; this version posted June 5, 2020. The copyright holder for this preprint (which was not certified by peer review) is the author/funder. All rights reserved. No reuse allowed without permission.

